

1 Long-Term Atmospheric Emissions for the Coal Oil Point 2 Natural Marine Hydrocarbon Seep Field, Offshore California

3 Ira Leifer¹, Christopher Melton¹, Donald R. Blake²

4 ¹Bubbleology Research International, Solvang, CA 93463, United States

5 ²University of California, Irvine, Department of Chemistry, Irvine, CA 92697, United States

6 Correspondence to: Ira Leifer (Ira.Leifer@bubbleology.com)

7 **Abstract.** In this study, we present a novel approach for assessing nearshore seepage atmospheric emissions through
8 modeling of air quality station data, specifically, a Gaussian plume inversion model. Three decades of air quality
9 station meteorology and total hydrocarbon concentration, *THC*, data were analysed to study emissions from the Coal
10 Oil Point marine seep field offshore California. *THC* in the seep field directions was significantly elevated and
11 Gaussian with respect to wind direction, θ . An inversion model of the seep field, θ -resolved anomaly, $THC'(\theta)$,
12 derived atmospheric emissions. The model inversion is for the far field, which was satisfied by gridding the sonar
13 seepage and treating each grid cell as a separate Gaussian plume. This assumption was validated by offshore *in situ*
14 offshore data that showed major seep area plumes were Gaussian. Of plume Total Carbon, *TC*, ($TC=THC$ +carbon
15 dioxide, CO_2 +carbon monoxide) 18% was CO_2 and 82% was *THC*; methane. 85% of *THC* was CH_4 . These
16 compositions were similar to the seabed composition, demonstrating efficient vertical plume transport of dissolved
17 seep gases. Air samples also measured atmospheric alkane plume composition. The inversion model used observed
18 winds and derived the three-decade-average (1990-2021) field-wide atmospheric emissions of $83,400 \pm 12,000 \text{ m}^3 \text{ THC}$
19 d^{-1} ($27 \text{ Gg THC yr}^{-1}$ based on 19.6 g mole^{-1} for *THC*). Based on a 50:50 air to seawater partitioning, this implies seabed
20 emissions of $167,000 \text{ m}^3 \text{ THC d}^{-1}$. Based on atmospheric plume composition, C_1 - C_6 alkane emissions were 19, 1.3,
21 2.5, 2.2, 1.1, and 0.15 Gg yr^{-1} , respectively. If CH_4 emissions were dispersed over the $\sim 6.3 \text{ km}^2$ of $25 \times 25 \text{ m}^2$ bins with
22 sonar values above noise, we find $5.7 \mu\text{M m}^{-2} \text{ s}^{-1}$. The approach can be extended to derive emissions from other
23 dispersed sources such as landfills, industrial sites, or terrestrial seepage if source locations are constrained spatially.

24 25 1 Introduction

26 1.1 Seepage and methane

27 On decadal timescales, the important greenhouse gas, methane, CH_4 , affects atmospheric radiative balance far more
28 strongly than carbon dioxide, CO_2 (IPCC, 2007, Fig. 2.21), yet CH_4 has large uncertainties for many sources (IPCC,
29 2013) and is very sensitive to hydroxyl (OH) concentration, the primary CH_4 loss mechanism (Y. Zhao et al., 2020).
30 Since pre-industrial times, CH_4 emissions have risen by a factor of ~ 2.5 , and after stabilizing in the 1990s and early
31 2000s, resumed rapid growth since 2007 (Nisbet et al., 2019). The significantly shorter lifetime of CH_4 than CO_2
32 argues for CH_4 regulatory priority as emission reductions (and changes to the radiative balance) manifest more quickly
33 as atmospheric concentrations decrease (Shindell, Faluvegi, Bell, & Schmidt, 2005). Further impetus for a CH_4 focus

34 is a recent estimate that 40% CH₄ emissions reductions are feasible at no net cost for the oil and gas, O&G, industry
35 (IEA, 2020), a major anthropogenic CH₄ source (IPCC, 2014). This is particularly salient given a recent estimate that
36 half of recent CH₄ increases are from the O&G industry (Jackson et al., 2020).

37
38 For 2008-2017, global CH₄ top-down emissions estimates are 576 Tg yr⁻¹; 1 Tg=10¹² g, range 550-594 Tg yr⁻¹, whereas
39 bottom-up approaches find 737 Tg yr⁻¹, range 594-881 Tg yr⁻¹ (Saunio et al., 2020). A significant fraction of this
40 discrepancy arises from uncertainty in OH concentration trends and spatial variability (Y. Zhao et al., 2020).
41 Anthropogenic sources for 2008-2017 were estimated at 336-376 Tg CH₄ yr⁻¹ based on bottom-up estimates. Natural
42 sources include wildfires, wetlands, hydrates, and geological seepage. Bottom-up estimates for natural sources are
43 higher than top-down estimates including for geological sources (Saunio et al., 2020). Geological sources (including
44 seepage) are estimated at 63-80 Tg CH₄ yr⁻¹ of which marine seepage is estimated to contribute 20-30 Tg CH₄ yr⁻¹
45 (Etiope, Ciotoli, Schwietzke, & Schoell, 2019) or 5-10 Tg CH₄ yr⁻¹ (Saunio et al., 2020). For comparison, marine
46 non-geological CH₄ emissions are estimated at 4-10 Tg yr⁻¹. The broad range of this estimate arises from the
47 uncertainty in the fraction of seabed emissions that reaches the atmosphere and the uncertainty in overall seabed
48 emissions. Further complexity in assessing geological seepage CH₄ emissions arise because both seepage and O&G
49 emissions source from the same geological reservoirs (Leifer, 2019) and thus are isotopically similar (Schwietzke et
50 al., 2016).

51
52 Seepage is process by which petroleum hydrocarbon gases and fluids in the lithosphere migrate to the hydrosphere
53 and/or atmosphere from a reservoir formation which underlies a capping layer that seals the formation, allowing
54 hydrocarbon accumulation. Thus, seepage requires a migration pathway, typically fracture and/or fault networks,
55 through the capping rock layer(s) (Ciotoli, Procesi, Etiope, Fracassi, & Ventura, 2020) or where the capping layer has
56 eroded away, as an outcropping of the reservoir formation (Abrams, 2005).

57
58 Marine seepage is widespread in every sea and ocean (Judd & Hovland, 2007) and occurs primarily (but not
59 exclusively) in petroleum systems and mostly in convergent basins (Ciotoli et al., 2020). Quantitative seepage
60 estimates (for global budgets) are limited (though growing); see Leifer (2019) review and below for more recent.
61 Fluxes for individual marine seep vents and seep areas have been reported for the Gulf of Mexico (C. Johansen et al.,
62 2020; Caroline Johansen, Todd, & MacDonald, 2017; Leifer & MacDonald, 2003; Römer et al., 2019; T. C. Weber et
63 al., 2014), the Black Sea (Greinert, McGinnis, Naudts, Linke, & De Batist, 2010), the southern Baltic Sea (Heyer &
64 Berger, 2000), various sectors of the North Sea (Borges, Champenois, Gypens, Delille, & Harlay, 2016; Leifer, 2015;
65 Römer et al., 2017), offshore Norway (Muyakshin & Sauter, 2010; Sauter et al., 2006) offshore Svalbard in the
66 Norwegian Arctic (Veloso-Alarcón et al., 2019), offshore Pakistan (Römer, Sahling, Pape, Bohrmann, & Spieß, 2012),
67 the arctic Laptev Sea (Leifer, Chernykh, Shakhova, & Semiletov, 2017), the East Siberian Arctic Sea (Shakhova et
68 al., 2013), the South China Sea (Di, Feng, Tao, & Chen, 2020), New Zealand's Hikurangi Margin (Higgs et al., 2019),
69 the Cascadia Margin (Riedel et al., 2018), and the Coal Oil Point (COP) marine hydrocarbon seep field, hereafter COP

70 seep field, in the northern Santa Barbara Channel, offshore Southern California (Hornafius, Quigley, & Luyendyk,
71 1999), and for numerous individual vents in the field (Leifer, 2010).

72
73 Most seep emission estimates are snapshot values from short-term field campaigns. Seep emissions vary on timescales
74 from tidal (Leifer & Boles, 2005; Römer, Riedel, Scherwath, Heesemann, & Spence, 2016) to seasonal (Bradley,
75 Leifer, & Roberts, 2010) to decadal (Fischer, 1978; Leifer, 2019). Additional temporal variability arises from transient
76 emissions – pulses lasting seconds to minutes (Greinert, 2008; Schmale et al., 2015) to decades (Leifer, 2019). This
77 shortcoming is being addressed by benthic (seabed) observatories and cabled observatories, e.g., Wiggins, Leifer,
78 Linke, and Hildebrand (2015); Greinert (2008), Kasaya et al. (2009); Römer et al. (2016); Scherwath et al. (2019).
79 Still, benthic observatories are costly and thus uncommon.

80
81 Seepage contributes to oceanographic budgets and to a lesser extent, to atmospheric budgets due to water column
82 losses with significant uncertainty in the partitioning. As a result, uncertainty in the atmospheric contribution is much
83 larger than the (significant) uncertainty in seabed emissions. Seepage partitioning between the atmosphere and ocean
84 - where microbial degradation occurs on timescales inversely related to concentration (Reeburgh et al., 1991), depends
85 primarily on depth (Leifer & Patro, 2002) with little to none of deepsea seabed emissions reaching the atmosphere,
86 e.g., Römer et al. (2019). In contrast, very shallow seepage (meter scale) largely entirely reaches the atmosphere both
87 by direct bubble-mediated transfer and diffusive transport. For intermediate depths, the ocean/atmospheric
88 partitioning is complex and depends on depth, bubble flux, bubble size distribution, bubble interfacial conditions, and
89 other characteristics (Leifer & Patro, 2002). Whereas the indirect diffusive flux (proximate and distal) depends on
90 bubble dissolution depth (Leifer & Patro, 2002), vertical turbulence transport in the winter wave-mixed layer (Rehder,
91 Keir, Suess, & Rhein, 1999), microbial oxidation losses, and exchange through the sea-air interface.

92
93 A range of approaches have been used to estimate the sea-air flux. The most common is by measuring the atmospheric
94 and water concentrations and applying air-sea gas exchange theory for the measured wind speeds, e.g., Schmale,
95 Greinert, and Rehder (2005) for Black Sea seepage under weak wind speeds. Sea-air exchange is a diffusive turbulence
96 transfer process that depends on the air-sea concentration difference and the piston velocity, k_T , which depends on gas
97 physical properties, wind speed, u (Liss & Duce, 2005), wave development (D. Zhao, Toba, Suzuki, & Komori, 2003)
98 including wave breaking (Liss & Merlivat, 1986), and surfactant layers at low wind speeds that suppress gas exchange
99 (Frew et al., 2004). k_T increases rapidly and non-linearly with u and has been parameterized by piecewise linear
100 functions (Wanninkhof, Asher, Ho, Sweeney, & McGillis, 2009) or by a cubic function (Nightingale et al., 2000). Air-
101 sea gas exchange theory is for (relatively) homogeneous atmospheric and oceanographic fields (concentrations, winds,
102 and wave development), and thus is inappropriate for point-source (bubble-plume) emissions and for the near-field
103 downcurrent plume, which tend to be heterogeneous.

104
105 Another approach uses seabed bubble size measurements or an assumed bubble size distribution to initialize a
106 numerical bubble propagation model to predict direct bubble-mediated atmospheric fluxes (Leifer et al., 2017; Römer

107 et al., 2017; Schneider von Deimling et al., 2011). The dissolved portion that evades to the atmosphere could be
108 addressed by a dispersive model coupled to an air-sea gas exchange model, though studies have not yet addressed this
109 component.

110
111 An alternate approach is to derive atmospheric emissions by plume inversion. Leifer, Luyendyk, Boles, and Clark
112 (2006) derived emissions for a blowout from Shane Seep in the COP seep field by a plume inversion. This neglected
113 the portion that dissolves during bubble rise and drifts downcurrent, out of the bubble plume's vicinity before sea-air
114 gas transfer into the atmosphere. Note dissolved gas evasion in the plume vicinity contributes to the inversion
115 emissions estimate.

116

117 **1.2 Study motivation**

118 In this study, we present a novel approach for assessing nearshore seepage atmospheric emissions – air quality station
119 data modeling, specifically using a Gaussian plume inversion model. This model requires that source locations are
120 mapped, spatially stable, and lie within a fairly constrained distance range band. These conditions are met for the COP
121 seep field, which is near the West Campus air quality Station (WCS). COP seep field lies in shallow coastal waters of
122 northern Santa Barbara Channel, CA. Spatial constraint is provided by geological structures, such as faults, that
123 constrain emission locations. The Gaussian plume model assumes a far-field source, whereas WCS is in the nearfield
124 of the extensive COP seep field. To satisfy the far field criterion, the source was gridded and each grid cell's emissions
125 treated as a distinct (distant) Gaussian plume. This characterization was validated in an offshore survey of several
126 focused COP seep field seepage areas, which were well-modeled as Gaussian plumes.

127

128 Thus, this study demonstrates an approach to deriving emissions from air quality station data for an area source such
129 as natural marine seepage. This approach could be used to derive emissions from other dispersed sources such as
130 landfills, industrial sites, or natural terrestrial seepage where the source locations are constrained spatially.

131

132 **1.3 Water column marine seabed seepage fate**

133 Seep seabed CH₄ partitioning between the atmosphere and water column depends on seabed depth and emission
134 character – as bubbles, bubble plumes (Leifer & Patro, 2002), or dissolved CH₄. Dissolved CH₄ migration through the
135 sediment is oxidized largely by near seabed microbes (Reeburgh, 2007), termed the microbial filter, negating its
136 contribution, leaving only bubble-mediated flow.

137

138 As seep bubbles rise, they dissolve, losing gas to the surrounding water at a rate that decreases with time. Smaller and
139 more soluble gases dissolve faster than larger and less soluble gases, i.e., fractionation (Leifer & Patro, 2002).
140 Additionally, larger bubbles transport their contents upwards more efficiently than smaller bubbles (Leifer et al.,
141 2006). Sufficiently large bubbles reach the sea surface with a significant fraction of their seabed CH₄ from depths of

142 even hundreds of meters (Solomon, Kastner, MacDonald, & Leifer, 2009). There are synergies, too with higher plume
143 fluxes driving a stronger upwelling flow that transports plume fluids with dissolved gases upwards towards the surface
144 where air-sea gas exchange drives evasion (Leifer, Jeuthe, Gjørund, & Johansen, 2009). Another synergy arises from
145 elevated dissolved plume CH₄ concentration (Leifer, 2010; Leifer et al., 2006), which slows dissolution. Also, bubbles
146 are oil-coated, which slows dissolution.

147
148 Moreover, gases in bubbles that dissolve in the wave-mixed layer (or reach it by the upwelling flow) then diffuse to
149 the air-sea interface due to wave and wind turbulence. Note, microbial degradation removes a portion of the dissolved
150 CH₄, which therefore never reaches the air-sea interface. Thus, there are two timescales that govern the fraction that
151 evades – the microbial degradation timescale, which increases as concentrations decrease, and the diffusion timescale,
152 which decreases with increasing wind speed. As a result, there is a dissolved plume that drifts downcurrent, with
153 evasion from this drifting plume creating a linear-source atmospheric plume. Note, dissolved plume concentrations
154 slowly decrease with time (downcurrent distance) from sea-air gas exchange losses, microbial oxidation, and
155 dispersion, leading to a decreased atmospheric plume.

156

157 **1.4 Atmospheric Gaussian plumes**

158 Strong focused atmospheric plumes are created from seep plume bubbles bursting at the sea surface and from dissolved
159 gas evasion within the bubble surfacing footprint. This evasion is enhanced by water-side turbulence from rising and
160 bursting bubbles (Leifer et al., 2015). Atmospheric plume evolution is described by the Gaussian plume model (Hanna,
161 Briggs, & Hosker Jr., 1982), which relates downwind concentrations to wind transport and turbulence dispersion and
162 is the basis of the inversion calculation (see Supp. Sec. S1 for details).

163

164 **1.5 Setting**

165 **1.5.1 The Coal Oil Point seep field**

166 The COP seep field (Fig. 1) is one of the largest seep fields in the world, with estimated 1995-1996 seabed total
167 hydrocarbon, *THC*, emissions, E_B , of $1.5 \times 10^5 \pm 2 \times 10^4$ m³ d⁻¹ (Hornafius et al., 1999). Hereafter emissions and
168 concentrations are for *THC* unless noted. Clark, Washburn, Hornafius, and Luyendyk (2000) estimated that half the
169 COP seep field E_B reach the atmosphere in the near field. This is due to shallowness, bubble oiliness, high plume
170 bubble densities, and turbulence mixing within the wave mixed layer.

171

172 Geological structures play a critical role in the spatial distribution of seepage (Leifer, Kamerling, Luyendyk, & Wilson,
173 2010), which lies along several trends in waters from a few meters to ~85 m deep. These trends follow geologic
174 structures including anticlines, synclines, and faults in the reservoir formation, the Monterey Formation and overlying
175 Sisquoc Formation. Faults and fractures associated with damage zones provide migration pathways with seepage
176 scattered non-uniformly along the trends, including focused seep areas that are highly active, localized, and often are

177 associated with crossing faults and fractures (Leifer et al., 2010). Seepage in these areas typically surrounds a focus
178 and decreases with distance, primarily along linear trends (Leifer, Boles, Luyendyk, & Clark, 2004). See Supp. Table
179 S3 for informal names and locations of selected focused seep areas.

180

181 **1.5.2 Coal Oil Point seep field emissions and composition**

182 COP seep field sources from the South Ellwood oil field whose primary source rock is Monterey Formation, which is
183 immature to marginally mature. Petroleum gases from marine organic materials have relatively higher proportion of
184 ethane, propane, butane, etc., relative to methane as compared to petroleum gases from terrestrial organic materials.
185 The wet gas fraction (C_2-C_5/C_1-C_5) indicates a thermogenic origin of greater than 0.05 (Abrams, 2017). Of the
186 saturated alkanes, the alkenes (olefins) are of biological origin. Additionally, the ethane/ethene ratio and
187 propane/propene ratios can be indicators of seep gas biogenic modification with values above 1000 indicating purely
188 thermogenic origin (Abrams, 2017; Bernard, Brooks, & Zumberge, 2001).

189

190 In this study, we analyse WCS (located at 34° 24.897'N, 119° 52.770'W) atmospheric *THC*. Clark, Washburn, and
191 Schwager (2010) report average seep field seabed CH_4 , CO_2 , and non-methane hydrocarbons (NMHC), of 76.7, 15.3,
192 and 7.7%, respectively, with Trilogy Seep seabed compositions of 67, 21, and 7.8%, respectively. With respect to
193 alkanes, seabed bubbles are 90.4% CH_4 and 8.6% NMHC. CO_2 rapidly escapes the bubbles and is negligible (<1%)
194 at the sea surface. At the sea surface, CH_4 in bubbles is ~90% with NMHC making up the remaining 10%, neglecting
195 air gases (Clark et al., 2010). Note, whereas seep *THC* is predominantly CH_4 , *THC* from terrestrial directions arises
196 from NMHC from traffic and other anthropogenic sources as well as CH_4 from pipeline leaks, terrestrial seeps, etc.

197

198 **1.5.3 Northern Santa Barbara Channel climate**

199 Diurnal and seasonal wind cycles are important to the atmospheric transport of COP seep field emissions. The Santa
200 Barbara climate is Mediterranean with a dry season and a wet seasons when storms occur infrequently (Dorman &
201 Winant, 2000). The semi-permanent eastern Pacific high-pressure system plays a dominant controlling role in weather
202 in the Santa Barbara coastal plain. This high-pressure system drives light winds and strong temperature inversions that
203 act as a lid that restricts convective mixing to lower altitudes. The coastal California boundary layer is shallow, from
204 0 to 800 m thick (Edinger, 1959); generally 240-300 m around Santa Barbara (Dorman & Winant, 2000). Additionally,
205 coastal mountains provide physical barriers to transport (Lu, Turco, & Jacobson, 1997).

206

207 As a coastal environment, the land/sea breeze is important to overall wind-flow patterns with weak offshore night
208 winds and stronger onshore afternoon winds (Dorman & Winant, 2000). In coastal Santa Barbara, warming on
209 mountaintops and more interior arid lands relative to cooler marine temperatures drives the sea breeze. Downslope
210 nocturnal flows warm nocturnal surface temperatures, moderating the coastal diurnal temperature cycle (Hughes, Hall,
211 & Fovell, 2007).

212
213 Typical morning winds are calm and offshore and often accompanied by a cloud-filled marine boundary layer, 50–
214 150 m thick (Lu et al., 1997). The marine layer usually (but not always) “burns off” mid-morning after which
215 temperatures rise, the boundary layer thickens and winds shift clockwise from offshore to eventually prevailing
216 westerlies aligned with the coastal mountains. Midday through late afternoon and even evening, winds strengthen,
217 often leading to whitecapping before the boundary layer collapses and winds return to the nocturnal pattern.
218

219 **2 Methods**

220 **2.1 West Campus Station data**

221 WCS data includes wind speed, u , and direction, θ , by a vane anemometer (010C,020C, Met One, Grants Pass, OR)
222 and THC concentration, C , by a Flame Ionization Detector (51i-LT, Thermo Scientific, MA). WCS is maintained by
223 the Santa Barbara County Air Pollution Control District. Daily instrument calibration occurs after midnight, rendering
224 C unavailable 00:50 to 02:09 local time, LT. WCS was improved significantly in 2008 from 1-hour to 1-minute time
225 resolution, which allowed far higher values of C and u due to the shorter averaging times. Data analysis uses custom
226 routines as well as standard routines and functions in MATLAB (MathWorks, MA).

227
228 First, WCS data were quality controlled to remove all values of C during the daily calibration, as well as to interpolate
229 neighboring values that were unrealistically low, i.e., C less than 1.6 ppm in the 1990s and 1.85 ppm in the 2000s.
230 Data since 2008 were smoothed by nearest-neighbor averaging, yielding 3-minute time resolution. Data prior to 2008
231 were hourly and were not smoothed. Wind data were nearest-neighbor averaged after decomposing into north and east
232 components, followed by recalculation of u and θ .

233

234 **2.2 *In situ* marine surveys**

235 Offshore *in situ* survey data were collected by the *F/V Double Bogey*, a 12-m, 9-ton, fishing vessel with a near
236 waterline deck (~0.2 m) and low overall profile (cabin at ~2.2 m). A sonic anemometer (VMT700, Vaisala) was
237 mounted on a 6.5-m tall, 5-cm (2”) diameter aluminum mast and measured 3D winds. Continuous, CH_4 and CO_2 data
238 were collected 5 Hz by a Cavity Enhanced Absorption Spectroscopy (CEAS) analyzer (FGGA, LGR Inc., San Jose,
239 CA). Vessel location and time were from a Global Positioning System (GPS) at 1 Hz (19VX HVS, Garmin, KS). CH_4
240 and CO_2 calibration with a greenhouse gas air calibration standard (CH_4 : 1.981 ppmv; CO_2 : 404 ppmv, Scott Marin,
241 CA, purchased 2015, Sigma Aldrich, St Louis, MO).

242

243 Data are real time integrated and visualized in Google Earth on a portable computer (Spectre360, HP) using custom
244 software, written in MATLAB (MathWorks, MA) that is described elsewhere (Leifer, Melton, Fischer, et al., 2018;
245 Leifer, Melton, Manish, & Leen, 2014; Leifer, Melton, Tratt, et al., 2018; Leifer et al., 2016). Real-time visualization

246 facilitates adaptive surveys, wherein the survey route is modified based on real-time data to improve outcomes
247 (Thompson et al., 2015) - in this case to facilitate plume tracking and to ensure transects were near orthogonal to the
248 wind.

249
250 Accurate, absolute winds are calculated from relative winds after accounting for vessel motion and filtering for non-
251 physical velocity changes due to GPS uncertainty (Leifer, Melton, Fischer, et al., 2018). Filtering removes transient
252 winds that are not relevant to plume transport. The filter interpolates GPS positions flagged as unrealistic.

253
254 Whole air samples were collected in evacuated 2-liter stainless steel canisters, which were filled gently over ~1 minute
255 from ~1 m above the sea surface. The filled canisters were analyzed in the Rowland/Blake laboratory at the University
256 of California, Irvine for carbon monoxide, CO, CH₄, and C₂-C₇ organic compounds. Samples were analysed by a gas
257 chromatography multi-column/detector analytical system utilizing flame ionization detection.

258

259 **2.3 Seep plume emissions model**

260 The plume inversion model is a three-step process (Leifer, Melton, Fischer, et al., 2018; Leifer, Melton, Tratt, et al.,
261 2018; Leifer et al., 2016). Emissions from focused seep areas were derived from offshore data by first fitting Gaussian
262 function(s) to orthogonal transect C' data, termed the data model. C' is relative to C outside the plume, derived by
263 linear interpolation across the plume transect. The data model is derived by error minimization using a least-squares
264 linear-regression analysis (Curve fitting toolbox, MathWorks, MA). Next, the Gaussian plume model (Eqn. S1; Supp.
265 Figs. S1 and S2) is fit to the data model. Transect data are collected close to orthogonal to the wind direction and are
266 projected in the wind direction onto an orthogonal plane. See Leifer, Melton, Tratt, et al. (2018) for a validation study
267 of the plume inversion model by comparison with remote sensing-derived emissions (which are largely insensitive to
268 transport). The study found *in situ* and remote-sensing derived emissions agreed within 11%.

269

270 **2.4 Seep field emissions model**

271 The inversion model is based on gridding the seep field into numerous small additive Gaussian plumes that represent
272 the area emissions and was written in MATLAB (MathWorks, MA). This assumes that each sea-surface grid cell
273 contributes a Gaussian plume, an assumption that was tested during an offshore survey that collected meteorology and
274 *in situ* concentration data downwind of several active seep areas.

275

276 The definition of an area source versus a point source depends on the relevant length scales – an area source is well
277 approximated as a point-source plume if sufficiently downwind (far field), where the distance for “sufficiently
278 downwind” depends on the area source dimensions and meteorological conditions. Whereas WCS is near field for the
279 entire seep field plume, it is far field for the small plumes from each grid cell.

280

281 The area source was based on a Sept. 2005 sonar survey sonar return, ω , map (Fig. 1), see Leifer et al. (2010) for sonar
 282 survey details, data were re-analysed for this study. Simulations used sonar data gridded at a hybrid 22/56-m in a UTM
 283 coordinate system, with origin at WCS. Specifically, gaps in the 22-m map were filled from the 56-m map (Supp. Fig.
 284 S3). The probability distribution of ω was used to identify the noise level (Supp. Fig. S4) as in Leifer et al. (2010).

285
 286 The model calculates a Gaussian plume for $E_{i,j}$ for grid cell i and j , for each grid cell with ω above noise. $C'_{Sim}(x, y)_{i,j}$
 287 and for the observed wind-direction, θ , resolved wind, $u(\theta)$, for a typical Santa Barbara channel boundary layer,
 288 $BL=250$ m. The initial $E_{i,j}$ was calculated by scaling such that the integrated sonar return, $\int \omega(x, y)$, scales to
 289 $E_A=1.5 \times 10^5 \text{ m}^3 \text{ dy}^{-1}$, i.e., E_B from Hornafius et al. (1999). The Gaussian plume is calculated in a Cartesian coordinate
 290 system (Supp. Fig. S5A), rotated to θ , and the interpolated linearly to double the spatial resolution. Then, the rotated
 291 plume is regridded to UTM coordinates using the `ffgrid.m` function (Supp. Fig. S5B). Interpolation removes gaps in
 292 the regridded plume map. Then, the regridded plume is renormalized to ensure total mass is conserved before and
 293 after these operations. Rotated regridded plumes are translated to the seep field grid and added, yielding $C'_{Sim}(x, y)$,
 294 which is the simulated seep field plume anomaly (Supp. Fig. S5C).

295
 296 The model scans θ for the seep directions ($110^\circ < \theta < 330^\circ$) and calculates the simulated plume anomaly, $C'_{Sim}(\theta)$ at
 297 WCS, which is compared with the observed WCS concentration, $C'_{Obs}(\theta)$. Hereafter, C_{Obs} and C_{Sim} and their
 298 anomalies refer to values at WCS. $C'_{Obs}(\theta)$ is defined,

$$299 \quad C'_{Obs}(\theta) = C_{Obs}(\theta) - \min(C_{Obs}(\theta)) \quad (1)$$

300 with the minimum typically from the west in a direction with no known seepage. Specifically, $C'_{Obs}(\theta)$ was calculated
 301 by subtracting the minimum in the annualized observed $C_{Obs}(t, \theta)$ each year, t , after applying a 7-year running
 302 average.

303
 304 Emissions from suburban communities, light industry, and commercial centers enhance $C'_{Obs}(\theta)$ for the northwest to
 305 northeast (~ 330 - 30°). These terrestrial emissions were removed by fitting a Gaussian function to $C'_{Obs}(\theta)$ for
 306 $330^\circ < \theta < 30^\circ$ with the residual yielding $C'_{Obs}(\theta)$. This only affected $C'_{Obs}(\theta)$ for overlapping directions corresponding
 307 to the fields' eastern edge.

308
 309 Simulations were run at angular resolutions of 2° . Higher angular resolution produced small artifacts for the 22/56-m
 310 sonar grid while the 11-m sonar grid was overly sparse due to the distance between sonar tracks (Supp. Fig. S3A).

311
 312 The source is the ω map in units of decibels, whereas emissions are in units of moles $\text{m}^{-2} \text{ s}^{-2}$. Given that the relationship
 313 between ω and bubble density (emissions) is complex and non-linear (Leifer et al., 2017), there is poor agreement
 314 between $C'_{Sim}(\theta)$ and $C'_{Obs}(\theta)$. Thus, a correction function, $K(\theta)$, is applied to emissions for each grid cell along each
 315 θ , $E_{i,j}(\theta)$, and the model rerun. $K(\theta)$ is defined,

316
$$K(\theta) = C'_{obs}(\theta) / C'_{sim}(\theta). \quad (2)$$

317 Initially, $K(\theta) = 1$, but in subsequent iterations, $K(\theta)$ is scaled as in Eqn. 2. Because $K(\theta)$ weights closer seeps more
 318 than more distant seeps, a distance-varying correction function, $K(r, \theta)$, was calculated such that,

319
$$\int_{r=0}^{r=\infty} E_A(r, \theta) = \int_{r=0}^{r=\infty} K(r, \theta) E_A(r, \theta) dr \quad (3)$$

320 where r is distance from WCS. E_A from simulations for different northwards shifts of WCS were fit with a polynomial
 321 to derive the function form of $K(r)$. Accounting for off-axis plume contributions requires several iterations to achieve
 322 *Convergence*, which was defined,

323
$$Convergence = \frac{\sum C'_{sim}(\theta) \sum C'_{obs}(\theta)}{\sum C'_{obs}(\theta)}. \quad (4)$$

324 Iterations continued to *Convergence* of 1% or better – typically 4 to 5 iterations. Simulations suggest wind veering,
 325 ψ , was important, which was implemented by calculating $C'(\theta)$ and assigning it to $C'(\theta + \psi)$.

326

327 **3 Results**

328 **3.1 Offshore *in situ* surveys**

329 An offshore COP seep field survey measured *in situ* C_{CH4} and u on 28 May 2016. Data were collected from the Santa
 330 Barbara harbor (~7.5 km east of the seep field, Fig. 2A; Supp. Fig. S6) to offshore Naples, several kilometers west of
 331 the seep field. Overall winds were easterly with an onshore component near Campus Point flowing onto UCSB and a
 332 broad (6-km wide) offshore flow west of COP that shifts to along coast near Naples (Fig. 2A, white arrows). Observed
 333 winds veered ~10° from east to the west sides of the seep field, roughly comparable to the shift in coastline orientation.

334

335 Plumes are apparent downwind of major seeps, with the largest plume associated with the Trilogy Seep (Fig 2B).
 336 Strong plumes also are evident downwind of the La Goleta Seep and Patch Seep. Notably, the Seep Tent Seep plume
 337 was very weak. The Seep Tent Seep was the dominant seep area in the COP seep field from its appearance in June
 338 1973 (Boles, Clark, Leifer, & Washburn, 2001) until recent years.

339

340 Additionally, the offshore survey identified focused plumes from beyond the extent of the seep field's 2005-sonar
 341 map. Specifically in the Goleta Bay, which has been noted (Jordan et al., 2020), and offshore Haskell and Sands
 342 Beaches, an area with abandoned oil wells, and off Naples Point (Fig. 2A, red arrow).

343

344 Plume alkane C' were determined by the difference between two “background” air samples collected immediately
 345 outside the plume and three Trilogy Seep plume air samples. CH_4 was 88.5% of THC , with ethane, propane, and
 346 butane at 3.1%, 4.2%, and 2.8%, respectively, with pentane, hexane, and heptane at 1.11, 0.13, and 0.04%, respectively
 347 (Table 1). Mean THC molecular weight is 19.6 g mole⁻¹ based on a composition weighting. Branched alkanes were

348 detected, with 2-methylpentane and 3-methylpentane comprising 0.21%, each, as well as simple aromatics, e.g.,
349 benzene and toluene, with concentrations of 78 and 18 ppm, respectively.

350
351 The observed wet gas fraction, $\sum_{n=2}^5 C_n / \sum_{n=1}^5 C_n$ was 0.11 indicating a thermogenic origin, i.e., greater than 0.05
352 (Abrams, 2017) - and thus derived from marine organic materials. Although the olefins ethene and ethyne were
353 detectable at 0.02% and 0.004%, respectively, butene was not detected. These olefins primarily derive from microbial
354 processes (Abrams, 2017), thus, the ethane/ethyne ratio of 6200 strongly indicates a thermogenic source (Bernard et
355 al., 2001). Plume atmospheric CO₂ was elevated by 12 ppm, thus CO₂ was 18% of Total Carbon, *TC*, – defined *TC* =
356 *THC*+CO₂+carbon monoxide, CO. CO was elevated minimally in the plume, just 2 ppb. Given that CO₂ completely
357 dissolves from bubbles well before reaching the sea surface (Clark et al., 2010), this demonstrates efficient vertical
358 transport of dissolved seep gases to the sea surface.

359
360 Plumes for the Trilogy Seeps, La Goleta Seep, and Seep Tent Seep were inverse Gaussian plume modeled to derive
361 emissions for each plume. For the Trilogy Seeps, the average *u* across the plume was 5.9 m s⁻¹, insolation was full
362 sun, and the source height was set at 25 m based on Trilogy’s atmospheric plume being buoyant. Model surface
363 concentrations for Trilogy B plume are shown in Fig 2B. The other two seeps are far less intense and used a 1-m
364 source height.

365
366 *E* for Trilogy A was 1.28 Gg CH₄ yr⁻¹ (5600 m³ CH₄ d⁻¹), whereas Trilogy B and C contributed 0.06 and 0.07 Gg CH₄
367 yr⁻¹, respectively, for a total of 6200 CH₄ m³ d⁻¹. Note, plume origins and the sonar seep bubble plume locations do
368 not precisely match because the sonar map is for near the seabed, and currents deflect the bubble surfacing location,
369 up to ~40 m. La Goleta Seep released 4000 m³ CH₄ d⁻¹ and the Seep Tent Seep released 310 m³ CH₄ d⁻¹ with almost
370 no surface bubble expression. For comparison, Clark et al. (2010) used a flux buoy, which measures near surface
371 bubble fluxes, and found Trilogy Seep emissions of 5500 and 4200 m³ THC d⁻¹ and 930 m³ THC d⁻¹ for La Goleta
372 Seep in 2005 and 5700 m³ THC d⁻¹ for the Seep Tent Seep in 2002. During the cruise, surface bubble plumes were
373 not observed for the Seep Tent Seep, although its bubble plume had been a perennial and dominant feature since its
374 appearance. Note, Clark et al. (2010) reported *THC* in near sea surface bubbles was 91% CH₄.

375

376 **3.2 West Campus Station**

377 **3.2.1 Temporal trends**

378 WCS is 500 m from the coast (to the southwest) at 11-m altitude and 850 m almost due south to the 11-m altitude
379 bluffs of Coal Oil Point (Fig. 1). Terrain slopes gently towards the coast to the southwest and towards a lagoon to the
380 south-southeast, rising again to the southeast to the COP bluffs. This flat relief likely has small to negligible effect on
381 wind speed and direction, although differential land-ocean heating could influence winds. Wind veering is likely for
382 the coast to the east of COP due to the orientation of the coastline and bluffs.

383

384 The WCS improvements in 2008 (Fig. 3-dashed line) allowed for higher values of C and u (Supp. Fig. S7A, S7B).
385 Comparison of the probability distributions of u and C , $\phi(u)$ and $\phi(C)$, respectively, before and after the upgrade did
386 not suggest biases were introduced (Supp. Fig. S7C, S7D). Specifically, changes in the average and median values
387 and in the baseline after 2008 were from better measurement of higher value events (gusts and short positive C
388 anomalies).

389
390 Significant daily, seasonal, and interannual variations are apparent in the day-averaged u and C (Fig. 3). The calmest
391 season is late summer to fall, whereas spring is the windiest and most variable due to synoptic systems (Fig. 3A).
392 Winds have strengthened since a minimum in 1995-1996, more so for the seep directions with stronger winds becoming
393 more frequent and more so for summer than winter (Supp. Figs. S8, S9).

394
395 Trends in C reflect trends in both seep field emissions and ambient C . C is higher in fall and spring (Fig. 3B). Given
396 that stronger winds decrease C through dilution, this suggests the seasonal variation in C underestimates the seasonal
397 variation in emissions. Several studies have shown increased emissions under higher wave regimes (storminess),
398 reviewed in Leifer (2019) and proposed from wave pumping. Storms increase evasion from higher wave turbulence
399 and breaking-wave bubbles, which sparge dissolved CH_4 and other trace gases down to the seabed in shallow (<100
400 m) waters (Shakhova, Semiletov, Salyuk, et al., 2010). Note, u , θ , and C' correlate with time of day. For example,
401 north generally reflects weak, offshore nocturnal winds with no seep contribution.

403 3.2.2 Spatial heterogeneity

404 Calculating the angular-resolved average C , $C_{ave}(\theta)$, for the complete dataset with respect to θ shows the highest C
405 from the main seep field direction (155-250°, Fig. 4). For the seep directions, $C_{ave}(\theta)$ was poorly fit by a single
406 Gaussian function but well fit ($R^2 = 0.997$) by two Gaussian functions with peaks at 178° and 198° corresponding to
407 the Seep Tent and Trilogy Seeps' directions, respectively (Figs. 4A, 4B). Notably, the fit residual showed a linear
408 increasing trend, $dC_{ave}(\theta)/d\theta$, of 0.17 ppb degree⁻¹ from 180 to 210° (Supp. Fig. S9B) consistent with evasion from
409 a dissolved downcurrent plume that drifts west-northwest along the coast (Leifer, 2019).

410
411 The average C anomaly, $C'_{ave}(\theta)$, was calculated from the average of $C_{obs}(\theta)$, after Eqn. 1, with terrestrial
412 anthropogenic sources to from the north to northeast removed. The minimum in $C_{obs}(\theta)$ was at 270°, a direction with
413 no mapped seepage that also is beyond the dissolved plume's approximate shoreward edge. Figs. 4A and 4B show
414 $C_{obs}(\theta)$ before removal of terrestrial emissions, which do not overlap in any significant manner with seep field
415 emissions.

416
417 There is a strong, focused peak in $C_{max}(\theta)$ at $\theta \sim 190^\circ$, close to the Seep Tent Seep direction (Figs. 4E, 4F), which is
418 fairly isolated on the offshore seep trend (Fig. 1). This peak also is close to the direction of Tonya Seep on the inshore
419 seep trend and to the small, unnamed area of seepage to the west of Trilogy Seep on the Red Mountain Fault trend.

420 The θ -resolved maximum $C(\theta)$, $C_{max}(\theta)$, remains elevated through $\sim 270^\circ$, far west of the $C_{ave}(\theta)$ peak at $\sim 200^\circ$.
 421 This strongly suggests that the seep field extends further to the west-northwest than current maps. These data cannot
 422 be explained by dissolved plume outgassing, which would affect $C_{ave}(\theta)$ but not $C_{max}(\theta)$.

423
 424 $C(\theta)$ enhancements for non-seep directions (Fig. 4A, 4B) show a peak at $\sim 35^\circ$, corresponding to the direction of a
 425 commercial center amid suburban development. This could result from terrestrial seepage and natural gas pipeline
 426 leakage and/or *THC* emissions from communities and traffic.

427
 428 Neglecting the synoptic system, topographic forcing from the east-west Santa Ynez Mtn. range means that the
 429 strongest winds are the prevailing westerlies (Fig. 4C, 4D). North winds (320 - 15°) largely are weak as are winds from
 430 due south; however, the sea breeze strengthens winds rapidly away from due south. θ peaks in the maximum winds
 431 (1-minute sustained), $u_{max}(\theta)$, correspond to the west and east peaks in $u_{ave}(\theta)$ with strengths to 16 m s^{-1} . Interestingly,
 432 there also are strong north (0 - 30°) winds or downslope flow, termed sundowner winds, a highly localized and
 433 infrequent phenomenon. The overlap of $u_{med}(\theta)$ and $u_{ave}(\theta)$ shows winds largely are normally distributed.

434
 435 The median C , $C_{med}(\theta)$, and average C , $C_{ave}(\theta)$, have similar shapes, albeit with lower values at all θ (Fig. 4A),
 436 indicating C is not normally distributed. This is shown in the wind direction-resolved wind speed probability
 437 distribution, $\phi(\theta, u)$ (Fig. 5A), defined such that

$$438 \int \phi(\theta, u) du = 1, \quad \int \phi(\theta, C) dC = 1. \quad (5)$$

439 $\phi(\theta, u)$ is very narrow (y-axis) for the northeast ($\sim 45^\circ$) where winds are largely weak and broad for the east-southeast
 440 (70 - 135°) and the prevailing westerlies (250 - 280°). The east-southeast distribution skews to the south (stronger winds
 441 extend further from the south - offshore), whereas the prevailing westerly wind distribution skews to the northeast (as
 442 does the coastline).

443
 444 In the seep direction, $\phi(C, \theta)$ extends to much higher values than from non-seep directions (Fig. 5B). $\phi(C, \theta)$ is
 445 asymmetric with θ extending further to the west than the seep field extent (240°) and then decreasing more abruptly
 446 than the decrease to the east. This asymmetry is expected given the seep field's asymmetric orientation relative to
 447 WCS (eastern seepage is more distant). Emissions beyond the field's mapped western edge arise from downcurrent
 448 plume outgassing and potentially contributions from unmapped seeps.

449

450 3.2.3 Seep field diurnal emissions cycle

451 C and u for the seep field direction, u_{seep} , and C_{seep} , respectively, follow diurnal patterns that are not the same as the
 452 overall diurnal pattern due to the wind direction constraint and because C_{seep} depends on u_{seep} . The dependency arises
 453 because higher u dilutes emissions, decreasing C , but higher u also increases dissolved plume evasion and bubble-
 454 mediated emissions from higher swell (after a delay for wave build-up). Diurnal winds in coastal regions feature a

455 shift between weak nocturnal offshore winds that veer to onshore winds in the morning - the sea breeze circulation.
456 This was explored in time and direction segregated u and C and seep direction averaged u_{seep} and C_{seep} for 90-270°
457 (Fig. 6). Data were segregated by θ for pre- and post-2008 (when station improvements facilitated better wind
458 characterization, particularly for night winds, which are seldom from the seep field direction, see Supp. Fig. S10 for
459 1991-2007). $u(\theta, t)$ and $C(\theta, t)$ were 2D Gaussian kernel smoothed with a 1-bin standard deviation (contours based on
460 a 3-bin standard deviation) by the `imgaussfilt.m` algorithm (MATLAB, MathWorks, MA) after interpolating the
461 calibration data gap 24:00-01:00.

462
463 Early morning (01:00–03:00) u_{seep} are stronger because typical nocturnal winds are northerlies (land breeze), coming
464 from the south largely during storms. These are accompanied by elevated C_{seep} implying greater emissions despite
465 enhanced dilution from stronger winds. The minimum in both u_{seep} and C_{seep} occur in the early morning (04:00-08:00),
466 with both increasing slightly through midday (~12:00). C_{seep} follows an afternoon trend of an overall decrease to a
467 minimum at ~20:00 before increasing into the late evening.

468
469 Underlying these trends are complex temporal spatial patterns. u for the north to northeast reaches a maximum around
470 noon and peak around 16:00; while C for northeast to east is low in the morning reaching a peak to the east in the
471 afternoon and likely reflects terrestrial sources. This pattern in $C(t, \theta)$ extends to nearly 130°. Beyond the seep field's
472 western edge, u is elevated from the prevailing direction (270°) with C elevated throughout the morning. There also
473 is a short-lived peak in u around noon at ~300°, which corresponds to a short-lived depressed C . These could be
474 consistent with wave development time, transport time, and sparging of the downcurrent plume; however,
475 interpretation based on these patterns largely is speculative.

476

477 3.3 Overall seep field emissions

478 3.3.1 Overall emissions

479 Average atmospheric emissions, E_A , for 1990-2020 were derived by an iterative Gaussian plume model, initialized
480 with the 2005 sonar map (Fig. 7A). An emissions sensitivity study on the effect of grid resolution was conducted for
481 resolutions from 11 to 225 m and a 22/56-m hybrid grid (Supp. Fig. S3). Simulations used moderate insolation to
482 derive the turbulence parameters and stability class (Supp. Fig. S2), a 250-m BL , typical of Santa Barbara Channel
483 marine values (Edinger, 1959; Rahn, Parish, & Leon, 2017), and 2° angular resolution (Hanna et al., 1982).
484 Simulations were run iteratively until convergence, typically within 5 iterations (Supp. Fig. S11). Sensitivity studies
485 found the distance weighting function, $K(r, \theta)$, was linear (Supp. Fig. S12).

486

487 Simulations could not reproduce observations in the Platform Holly direction ($\theta=238^\circ$). Thus, a source was added for
488 the platform area, which improved simulation-observational agreement in this wind direction. Since significant seep
489 bubbles plumes generally are not observed in the platform's vicinity, these emissions could arise from incomplete
490 combustion during flaring.

491
492 The model-derived, E_A , for 1990-2020 was 83,400 $\text{m}^3 \text{d}^{-1}$ (Fig. 7). Using a composition-weighted *THC* molecular
493 mass of 19.6 g mole^{-1} implies 27 Gg *THC* yr^{-1} . Atmospheric seep gas is 88.5% CH_4 , implying 19 Gg $\text{CH}_4 \text{ yr}^{-1}$ seep
494 emissions (Table 1). Given that CH_4 is 73% of *THC*, non-methane hydrocarbon (NMHC: $\text{C}_2\text{-C}_7$) emissions are 9,600
495 $\text{m}^3 \text{d}^{-1}$ and gases emissions of 6.0 Gg yr^{-1} . For reference, Santa Barbara County 2018 Reactive Organic Carbon (ROC)
496 emissions are listed at $\sim 27 \text{ tons d}^{-1}$ (9.9 Gg yr^{-1}) (ourair.org/emissions-inventory, SBAPCD). For our analysis NMHC
497 and ROC are the same. The largest NMHC was propane with emissions of 3510 $\text{m}^3 \text{d}^{-1}$, followed by ethane at 2590
498 $\text{m}^3 \text{d}^{-1}$. The NMHC components of *THC* are conservative (do not react significantly) on the typical transport timescales
499 from the seep field to WCS (20-30 minutes).

500
501 Seabed emissions, E_B , are necessarily significantly greater than E_A as E_A misses the fraction of emissions that remain
502 in the water column, E_W , at least in the field's near downcurrent. There are two notes, the model E_A includes evasion
503 from the dissolved plume in the area covered by the seep field sonar map. Secondly, the model does not include E_A
504 from the dissolved fraction that evades beyond the seep field extent. For the seep field area and near downcurrent area,
505 Clark et al. (2000) estimated a 50:50 air/water partitioning based on a field study, implying $E_B = 167,000 \text{ m}^3 \text{d}^{-1}$ for
506 1990-2020 (54 Gg yr^{-1}). A comparison of E_A versus ω showed a very steep increase with ω for $E_A = 1\text{-}10 \text{ g s}^{-1} \text{ m}^{-2}$ with
507 rollover at $\omega \sim 0.022$ (Supp. Fig. S13), which was approximately the noise level (Supp. Fig. S4).

508
509 Insights were provided by how the model partitioned emissions between different seep areas (Fig. 7). Particularly
510 notable is the model's treatment of the Trilogy Seep area - the second strongest seep area after the Seep Tent Seep
511 during the study period. The model re-assigned Trilogy Seep emissions to seepage to the west, representing Trilogy
512 Seep emissions as unrealistically weaker than other, smaller seeps, such as IV Super Seep. One likely contributor to
513 this re-assignment is wind veering (Supp. Fig. S14). Also suggesting wind veering is the model's assignment of strong
514 emissions to the field's eastern and western edges despite weak sonar returns. In a comparison of the Seep Tent Seep
515 and La Goleta Seep areas, the model emphasized the Seep Tent Seep whereas La Goleta Seep emissions were shifted
516 to inshore seepage. This re-partitioning was greatly reduced for a $+10^\circ$ wind veer, which also lessened the
517 strengthening of emissions from the field's western edge relative to sonar. Given the lack of field data between the
518 seep field and WCS on wind veering, further wind veering analysis was not conducted.

519

520 3.3.2 Seep field sector emissions

521 To investigate sub-field scale emissions, the seep field was segregated into three sectors: inshore, offshore east, and
522 offshore west (Fig. 1). Based on integrating sonar return, ω , inshore seepage contributes 40% of the field's ω with the
523 offshore seep trend split between 9% for the west and 51% for the east. Supporting this comparison is the similarity
524 in the normalized sonar return probability distribution, $\phi_n(\omega)$, for the inshore seeps and offshore east seeps (Fig. 8). In
525 contrast, $\phi_n(\omega)$ for offshore west seepage differed dramatically despite the similarity in geology along the anticline
526 underlying the offshore seep trend (Leifer et al., 2010). This likely results in part from the interaction between

527 migration and production from Platform Holly. Although the normalized atmospheric emissions probability
528 distribution, $\phi_i(E_A)$, for the inshore and offshore seeps are similar over most of the range (except the weakest, $E_A < 0.02$
529 g s^{-1}), significant differences are evident between offshore east and west seepage. Offshore east seepage is more
530 dispersed and favors weaker seepage compared to offshore west seepage.

531
532 The weakest seepage ($\omega < 0.02$) contributes negligibly to overall sonar return and had no notable inshore-offshore $\phi_i(\omega)$
533 difference (Fig. 8). The largest difference is between the strongest seepage ($\omega > 0.5$) for the inshore and offshore seeps.
534 Specifically, there is a strong peak at $\omega \sim 0.45$ and nothing stronger for the inshore seeps, whereas offshore $\phi_i(\omega)$
535 continued to $\omega \sim 0.7$. The E_A probability distribution, $\phi_i(E_A)$, for the strongest inshore seepage was similar to $\phi_i(E_A)$ for
536 strong offshore seepage. However, this masked a significant east-west offshore seepage difference. Specifically,
537 $\phi_i(E_A)$ for strong seepage was reduced far more for offshore east seepage than offshore west seepage, and the reverse
538 for weak seepage.

539
540 The similarities of these distributions suggest that the controlling geological structures (fractures, fault damage zones,
541 chimneys, etc.) are the same for inshore seepage and offshore east seepage, with the primary difference for the
542 strongest seepage in these two sectors which are of similar strength – the inshore Trilogy Seeps provide focused
543 emissions, whereas the offshore east La Goleta Seeps are comparatively dispersed and far oilier.

544
545 Although, ω is not E_A , E_A followed the 40:60 partition in ω between inshore and offshore seepage. Interestingly, the
546 E_A partitioning between the offshore east and offshore west differed significantly from sonar partitioning with 21% of
547 E_A from offshore west and 38% from offshore east. This greatly accentuated the E_A Seep Tent Seep area. In part, this
548 arises from a diurnal cycle bias – WCS observes the offshore west seeps for afternoon/evening westerly winds, which
549 are stronger, whereas WCS observes the offshore east seeps when winds are weaker, earlier in the day (Fig. 6B).
550 Winds increase bubble emissions from wave hydrostatic pumping and dissolved gas evasion. Also potentially
551 contributing is saturation of ω at very high bubble-density bubble plumes, such as the Seep Tent Seep and Trilogy
552 Seep (Leifer et al., 2017). Saturation would imply an under-estimate of ω for the strongest seep area emissions which
553 are for the west offshore seepage, altering the west: east ω ratio (9%:51%).

554

555 3.3.3 Uncertainty and emissions sensitivity

556 Given the number of sources with poorly characterized variability, uncertainty is best assessed by Monte Carlo
557 simulations; however, this was unfeasible due to the simulations' computational demands. Thus, emissions uncertainty
558 was investigated by sensitivity studies (Fig. 9). Where data were available, uncertainty due to a specific parameter
559 was estimated from the data. Specific parameters studied included sonar resolution, angular resolution, $\delta\theta$, wind speed,
560 u , concentration anomaly, C' , boundary layer height, BL , wind veering, ψ , spatial northing offset, Y , and the inshore
561 and offshore seepage partitioning, ζ . Sensitivity study details are presented in Supp. Sec. S7.4.

562
563
564
565
566
567
568
569
570
571
572

573

574
575
576
577
578

579
580
581
582
583
584

585
586
587
588
589
590
591

The contribution to uncertainty from $\delta\theta$, C' , ψ , and spatial offsets within the seep trends were minimal – just a few percent or less. Moderate uncertainty was identified for BL and ζ . For example, for BL ranging from 150 to 350 m, mean E_A uncertainty was 6%. Although u has strong sensitivity, combined with BL it does not as u counters BL – lower u corresponds to higher BL . There still is uncertainty, though in the value of BL , which is not measured. Assessing uncertainty in ζ was more challenging as there is no verification data on variability in the E_A partitioning between the inshore and offshore seep trends. The mean E_A uncertainty for $-50\% < \zeta < 50\%$ is 11.5% from a polynomial fit. Still, the consistency in seepage location between sonar surveys spanning decades (Leifer, 2019) suggests only modest changes in ζ over the multi-decade time period of model averaging. Total uncertainty was taken as 15% based on the sum of uncertainty in BL and ζ , each averaged to the nearest 5%.

3.4 Ellwood Field emissions

$C(\theta)$ increases to the northeast with a peak at 290-320° corresponding to the direction towards abandoned wells off Haskell Beach (Fig. 10). Emissions from this area – either from natural seepage or leaking wells – were noted in the offshore survey data near Haskell Beach (Fig. 2A). Additionally, $C_{max}(\theta)$ shows a 22-ppm peak in in this direction well above $C_{ave}(\theta)$ (Fig. 4F), consistent with transient releases from natural seep and/or abandoned well emissions.

Ellwood field production continued through the 1970s with wells drilled into the geological structures that allowed oil accumulation (Olson, 1983) including faults that provide migration pathways (Leifer et al., 2010). There are many abandoned wells from these oil fields and from others fields on the Goleta Plains, beaches, and shallow near-coastal waters to the west-northwest of WCS (offshore Haskell Beach and onshore around Naples Point). Currently, active wells only are found at the La Goleta Gas field (a natural gas storage field), east of WCS.

Faults associated with these anticlines provide migration pathways and are approximately aligned with the coast in a series of roughly parallel faults extending onshore (Minor et al., 2009). The onshore/coastal Ellwood field (northwest of the South Ellwood field) sources from the primarily sandstone Vaqueros Formation (Olson, 1983), whose main trap is an anticline at the western edge of the North Branch Western More Ranch Fault (NBWMRF). Offshore seepage tracks some of these faults, e.g., the Isla Vista Fault trend corresponds to an offshore seep trend in Goleta Bay that includes the Goleta Pier Seep, whereas wells follow the NBWMRF trend offshore of Haskell Beach.

592 4 Discussion

593 4.1 Atmospheric seep field observations

594 4.1.1. Air quality station

595 A range of approaches are available to evaluate marine seepage CH₄ emissions: *in situ* approaches including direct
596 capture (Leifer, 2015; Washburn, Johnson, Gotschalk, & Eglund, 2001), fluid flow measurements (Leifer & Boles,
597 2005), video (Leifer, 2015), and remote sensing approaches that include active acoustics, i.e., sonar (Hornafius et al.,
598 1999), dissolved *in situ* (Marinaro et al., 2006), and passive acoustics (Wiggins et al., 2015). Remote sensing is the
599 best approach for long-term monitoring to capture shifts in emissions between vents. To date, only sonar remote
600 sensing has provided quantitative seep plume (seabed) emissions. Notably, sonar ranges are up to a few hundred
601 meters, far less than the size scales of many seep fields, whereas high power demands typically require a cabled
602 observatory for long-term observations.

603
604 This study demonstrated that air quality station data can provide the long-term continuous data needed to capture
605 seasonal variations including emissions during storms and transient events, which field campaigns likely miss. For
606 example, sonar surveys generally are scheduled during summer when seas are calmer and winds more predictable and
607 when seepage is weakest (Fig. 3); however, not during storms when emissions likely are enhanced.

608
609 The approach derived atmospheric trace gas emissions for a dispersed area source constrained by sonar seepage maps
610 from long-term air quality and meteorology data. This approach can be extended to terrestrial seepage if the source
611 can be constrained spatially (due to geology); although nearby anthropogenic sources may complicate emissions
612 assessments. Other terrestrial sources such as landfills, O&G production fields, or industrial sites – if spatially
613 constrained – could be addressed by this approach, particularly if isolated from other confounding sources. The use
614 of cavity enhanced absorption spectrometers that can speciate gases like CH₄ and C₂H₆ that could enable
615 discrimination some confounding sources as well as better characterization of emissions. Although an onshore station
616 can address nearshore seepage, further offshore seepage could be addressed by a moored station. Moored stations also
617 could include *in situ* aqueous chemical sensors, current measurements.

618

619 4.1.2 *In situ* atmospheric surface surveys

620 Atmospheric emissions were assessed for three seep areas - zone of focused seepage - by an atmospheric *in situ* survey
621 approach wherein downwind data are collected orthogonal to the wind direction in a transect that spans the plume
622 (background to background on the plume's edges). This approach was developed for terrestrial sources (Leifer,
623 Melton, Tratt, et al., 2018) yet remains unused for offshore marine seepage, which often are area sources. In this study,
624 this was addressed by gridding the area source and treating each grid as a far-field point source. Gaussian plume
625 inversion requires distant source(s), i.e., far field. Downwind *in situ* transects of three strong seep areas all were well
626 characterized by the Gaussian plume model.

627
628 One advantage of atmospheric surveys is rapidity - a single transect of a few minutes is sufficient to derive emissions
629 for a seep area. In comparison, a flux buoy survey can require many hours to a day (Clark et al., 2010), during which
630 forcing factors (waves, tides, etc.) change significantly. Also rapid are seep area sonar surveys (Wilson, Leifer, &
631 Maillard, 2015) allowing a combined sonar and atmospheric survey to repeat characterize emissions and sea-air
632 partitioning within a few hours. With respect to the entire COP seep field, whereas a sonar survey requires two to
633 three days (Leifer et al., 2010), a downwind atmospheric survey is far more rapid, requiring perhaps an hour. This
634 allows repeat field emissions measurements over a tidal cycle.
635

636 **4.2 Seep field emissions**

637 **4.2.1 Total emissions**

638 To date, only two estimates of COP seep field seabed emissions, E_B , have been published. Hornafius et al. (1999)
639 estimated $E_B=1.5 \times 10^5 \text{ m}^3 \text{ dy}^{-1}$ (64 Gg yr⁻¹) based on sonar surveys covering 18 km² from Nov. 1994 – Sep. 1996,
640 collected during the summer to late fall seasons. This value excluded Seep Tent collection. A 4.1 km² sonar survey in
641 Aug.-Sep. 2016 estimated $E_B=24,000 \text{ m}^3 \text{ dy}^{-1}$ (Padilla, Loranger, Kinnaman, Valentine, & Weber, 2019), significantly
642 lower, which in part arises from field subsampling, but also could arise from long-term changes; however, neither
643 study addressed temporal variability. The sonar surveys occurred in summer and fall when seepage activity is at a
644 minimum, whereas winter and early spring feature much higher activity associated with large transient events and
645 storms (Bradley et al., 2010).

646
647 Hornafius et al. (1999) used an engineered bubble plume to calibrate emissions, an approach also used in Leifer et al.
648 (2017). Due to technology limitations at the time, the strongest seepage was clipped or saturated, i.e., underestimated,
649 and the survey did not cover shallow seepage. Thus, the Hornafius et al. (1999) emissions estimate is a lower limit for
650 summer/fall emissions. The Padilla et al. (2019) survey was calibrated by an inverted seep flux buoy suspended at 23
651 m. This differs significantly from the seep flux buoy measurement approach reported in Washburn et al. (2001), which
652 are collected in surface drift mode. Surface drift mode ensures a horizontal orientation for the buoy and an absence of
653 lateral velocity difference between the capture device and currents – either of which decreases capture efficiency from
654 100%, biasing derived emissions low. Further, the Padilla et al. (2019) survey was calibrated 1 month after the sonar
655 surveys, whereas the 1995 engineered plume calibration by Hornafius et al. (1999) was contemporaneous. The
656 Hornafius et al. (1999) approach accounts in part for dissolution between the seabed and survey depth window - it
657 used air rather than CH₄, which dissolves slower than CH₄. Dissolution losses for CH₄ between the seabed and the
658 depth window can be addressed by a numerical bubble model (Leifer et al., 2017).

659
660 The Gaussian plume model-derived E_A was $8.3 \times 10^4 \text{ m}^3 \text{ dy}^{-1}$. Based on the Clark et al. (2000) assessment that half the
661 seabed seepage reaches the atmosphere, $E_B=1.7 \times 10^5 \text{ m}^3 \text{ dy}^{-1}$; very similar to $E_B=1.5 \times 10^5 \text{ m}^3 \text{ dy}^{-1}$ from Hornafius et al.

662 (1999). This agreement is coincidental as it neglects seasonal and interannual trends. For example, Bradley et al.
663 (2010) found 1994-1996 emissions were well below the average for 1990-2008, increasing significantly after 2008.
664

665 **4.2.2 Methane and non-methane hydrocarbon emissions**

666 Analysis of atmospheric samples provided a picture of the complexity of atmospheric emissions that arises from the
667 multiple pathways underlying atmospheric emissions. Specifically, as bubbles rise, they lose lighter and more soluble
668 gases faster (deeper in the water column), leading to differences between evasion from dissolved gases and direct
669 bubble transport (Leifer & Clark, 2002). Thus, bubble-mediated transport enhances larger alkanes relative to smaller
670 alkanes leaving more of the smaller alkanes in the water column. For strong seeps, bubble plumes are associated with
671 strong upwelling flows (Leifer et al., 2009), which transport dissolved gases to the sea surface where they outgas.
672 Additionally, oil (as droplets and bubble coatings) enhances alkane transport due to slower dissolution and diffusion
673 of larger alkanes through oil.
674

675 Atmospheric plume concentrations were 11.5% *NMHC* and 88.5% CH_4 , very similar to Hornafius et al. (1999) who
676 referenced the Seep Tent composition (88% CH_4 , 10% *NMHC*, and 2% nitrogen) as very similar to the reservoir
677 composition. Note, Clark et al. (2010) observed Trilogy near sea surface bubbles with 5.7% to 7.9% *NMHC* and 52.4
678 to 79.7% CH_4 , demonstrating significant partitioning. The similarity between the atmospheric and seabed composition
679 despite the difference in the bubble composition demonstrates efficient dissolved gas transfer to the sea surface.
680

681 COP seep field seabed emissions are orders of magnitude greater than typically reported for other seep areas, e.g.,
682 summary Römer et al. (2017) where emissions for 12 different seep areas including sites in the North Sea, Pacific
683 northwest, Gulf of Mexico, etc., were 2-480 tons yr^{-1} , multiple orders of magnitude less than COP seep field seabed
684 emissions. Römer et al. (2017) used a bubble model for Dogger Bank seepage in the North Sea to estimate emissions
685 for observed atmospheric CH_4 plumes. The model estimated direct atmospheric bubble-mediated emissions of 21.7
686 ton yr^{-1} , 20% of seabed emissions. For the Tommelieten Seeps (in 70-m water) Schneider von Deimling et al. (2011)
687 estimated 4% of the 0.024 Gg $\text{CH}_4 \text{ yr}^{-1}$ seabed emissions, i.e., $\sim 1 \text{ Mg } \text{CH}_4 \text{ yr}^{-1}$ reached the atmosphere by bubble-
688 mediated transfer. Schneider von Deimling et al. (2011) used a bubble model based on an assumed bubble size and
689 neglected diffusive flux. These diffusive fluxes include bubble dissolution into the wave mixed layer in the local area.
690 A few studies have directly measured atmospheric fluxes by an air-sea gas transfer model. For example, Schmale,
691 Beaubien, Rehder, Greinert, and Lonmbardi (2010) found seep air fluxes of 0.96-2.32 $\text{nmol m}^{-2} \text{ s}^{-1}$, much higher than
692 the ambient Black Sea flux of 0.32-0.77 $\text{nmol m}^{-2} \text{ s}^{-1}$. In the Black Sea, ambient emissions arise from microbially
693 produced CH_4 in shelf and slope sediments (Reeburgh et al., 1991). Di, Feng, and Chen (2019) estimated 7.7 nmol m^{-2}
694 s^{-1} for the shallow South China Sea based on an air-sea gas transfer model. If we disperse COP seep field atmospheric
695 emissions of $1.15 \times 10^9 \text{ M yr}^{-1}$ over the $\sim 6.3 \text{ km}^2$ of $25 \times 25 \text{ m}^2$ bins with emissions, we find $5.7 \text{ } \mu\text{M m}^{-2} \text{ s}^{-1}$, three orders
696 of magnitude greater.
697

698 Recent estimates of total global geo-CH₄ sources from a bottom-up approach are 45 Tg yr⁻¹ with submarine seepage
699 contributing 7 Tg yr⁻¹ (Etioppe & Schwietzke, 2019), implying COP seep field contributes ~0.27% of global submarine
700 emissions. However, an estimate of pre-industrial CH₄ emissions (not confounded with fossil fuel production
701 emissions) based on ice core ¹⁴CH₄ suggested 1.6 Tg geo-CH₄ yr⁻¹ emissions (Hmiel et al., 2020). This estimate, if
702 accurate, would imply the COP seep field contributes an astounding 1% of global seep emissions (submarine and
703 aerial) and is difficult to reconcile with the COP seep field and other top seepage estimates. For example, CH₄
704 atmospheric emissions for the Lusi hydrothermal system of 0.1 Tg yr⁻¹ (Mazzini et al., 2021), a hotspot in the Laptev
705 Sea of 0.9 Tg yr⁻¹ into shallow seas (Shakhova, Semiletov, Leifer, et al., 2010), and for the East Siberian Arctic Sea
706 using eddy covariance of 3.0 Tg yr⁻¹ (Thornton et al., 2020). Thus, COP seep field emissions either play a significant
707 role in global seep emissions or indicate that geo-gas emissions are less tightly constrained.

708
709 COP seep field C₂H₆ emissions were 1.27 Gg C₂H₆ yr⁻¹. For reference, this is 11% of the 11.4 Gg C₂H₆ yr⁻¹ in 2010
710 for the South Coast Air Basin (SCAB), which includes Los Angeles (Peischl et al., 2013). Globally, Simpson et al.
711 (2012) and Höglund-Isaksson (2017) found 11.3 and 9.7 Tg C₂H₆ yr⁻¹ in 2010, respectively. C₂H₆ has been increasing
712 since 2010 due to increased O&G production emissions (Helmig et al., 2016). Globally, seeps are estimated to
713 contribute 2-4 Tg C₂H₆ yr⁻¹ (Etioppe & Ciccioli, 2009), and from ice cores, 2.2-3.5 Tg yr⁻¹ {Nicewonger, 2016 #3816}.
714 This suggests the COP seep field contributes 0.03-0.06% of global seep emissions.

715
716 Seep THC was 4.2% propane, implying emissions of 2.5 Gg C₃H₈ yr⁻¹. Global propane emissions are 10.5 Tg yr⁻¹
717 (Poizzer et al., 2010), with 1-2 Tg yr⁻¹ estimated for seeps (Etioppe & Ciccioli, 2009). This suggests the COP seep field
718 contributes 0.05-0.1% of the global seep budget. Oceans are estimated to contribute 0.35 Tg C₃H₈ yr⁻¹ (Poizzer et al.,
719 2010), less than geological seepage contribution.

720
721 Based on an evaluation of the COP seep field emissions with respect to global seep ethane and propane emissions,
722 COP seep field contribution to global geo-CH₄ emissions are consistent with recent global geo-gas CH₄ emissions
723 estimates of 45 Tg yr⁻¹ (0.04%) (Etioppe et al., 2019), not the significantly lower pre-industrial estimates of global geo-
724 CH₄ emissions, e.g., 1.6 Tg yr⁻¹ (1.15%) (Hmiel et al., 2020).

725
726 Global butane emissions are 14 Tg C₄H₁₀ yr⁻¹ (Poizzer et al., 2010), higher than ethane and propane. COP seep field
727 butane (C₄) and pentane (C₅) emissions were 2.2 Gg C₄H₁₀ yr⁻¹ and 1.1 Gg C₅H₁₂ yr⁻¹, respectively, with combined
728 C₂-C₅ emissions of 7.1 Gg yr⁻¹, compared to 65 Gg yr⁻¹ from the entire SCAB, i.e., COP seep field contributes ~5%
729 the SCAB. COP C₂-C₅ emissions are significantly above that of the La Brea area, estimated at 1.7 Gg yr⁻¹ (D. Weber
730 et al., 2017). Note, COP seep field atmospheric C₂-C₅ emissions certainly are larger, potentially significantly, as larger
731 alkanes also are emitted from oil slicks but were not considered for this study, and furthermore, the atmospheric plume
732 from the slicks was not sampled for this study.

733

734 Both benzene and toluene were detected with estimated emissions of 8300 and 2300 kg yr⁻¹, respectively. These
735 emissions likely are underestimates, potentially significantly, due to neglecting the oil slick evaporation contribution.
736 Both gases are of significant health concerns, as are alkanes like pentane and hexane.

737

738 **4.3 Downcurrent emissions**

739 The seep field concentration, $C'(\theta)$, anomaly was centered at $\theta \sim 200^\circ$ and well matched the location of the seep field,
740 and moreover, was well described by a dual Gaussian function (**Fig. 4B**). This was surprising given that the seep field
741 is asymmetric with respect to a 200° axial line from WCS to COP. Underlying this seeming discrepancy is that WCS
742 winds are weakest from due south and strongest from the west (prevailing) and also stronger to the east-southeast
743 (**Fig. 4C**).

744

745 The residual of the Gaussian fit increased in the downcurrent direction (**Supp. Fig. S9B**), consistent with evasion from
746 the downcurrent dissolved plume and seepage from this area. The dissolved plume roughly follows the coast,
747 extending as far as $\sim 280^\circ$ from WCS due to the coastline shift from northwest to west around Haskell Beach (**Fig. 10**),
748 $\sim 30^\circ$ beyond the seep field's sonar mapped western edge (**Fig. 1**). As prevailing winds are westerlies (paralleling the
749 coastal mountains), downcurrent plume evasions decrease with distance due to dispersion and also as surface waters
750 become depleted by evasion. Evasion increases non-linearly with u , particularly for winds that include wave breaking
751 (Nightingale et al., 2000); however, higher winds also dilute emissions. Note, there are no mapped seeps in this area.

752

753 Dissolved plume emissions also likely occur from east of the field, leading the model to emphasize seepage at the
754 field's eastern extent, too. Specifically, strong prevailing afternoon westerly surface winds drive a near-surface
755 dissolved plume eastwards. When these westerly winds calm down late in the evening, easterly winds transport
756 evasion from this east-displaced dissolved plume towards WCS. Additionally, it also is possible that the COP seep
757 field extends further east than mapped in sonar surveys, at least during some seasons.

758

759 **4.4 Focused seep area emissions**

760 Trilogy Seep area emissions were estimated at 6,200 m³ CH₄ dy⁻¹ in May 2016. For comparison, Clark et al. (2010)
761 found 5500 and 4200 m³ THC dy⁻¹ (4,900 and 3,700 m³ CH₄ dy⁻¹) for Trilogy Seep as measured by flux buoy for near
762 surface bubble fluxes in Sept. 2005. Note, the plume inversion approach also includes outgassing of near surface
763 waters that have enhanced C_{CH_4} from plume dissolution, which the flux buoy approach does not include. Although
764 Clark et al. (2010) found surface bubbles had undetectable CO₂, the atmospheric plume's CO₂ to CH₄ concentration
765 ratio was comparable to the seabed bubble concentration ratio. This demonstrates significant upwelling flow transport
766 of seabed water to the sea surface where dissolved gases evade near where the bubble plume surfaces. This near-plume
767 evasion contributes to the atmospheric plume. Note, these emissions neglect downcurrent emissions. A 50:50

768 atmosphere:ocean partitioning suggests 2016 Trilogy Seep emissions were ~40% lower than in 2005 – a difference
769 within the difference between the two 2005 Trilogy Seep measurements Clark et al. (2010).

770
771 In contrast, agreement was very poor for the Seep Tent Seep, for which Clark et al. (2010) mapped emissions of 5700
772 $\text{m}^3 \text{ day}^{-1}$ ($5000 \text{ m}^3 \text{ CH}_4 \text{ day}^{-1}$) in Nov. 2002 whereas this study found $310 \text{ m}^3 \text{ CH}_4 \text{ dy}^{-1}$. This discrepancy was readily
773 apparent with almost no visible surface bubble expression in May 2016, whereas the Seep Tent Seep has been a
774 perennial feature since its appearance. The absence of more than a few scattered bubbles at the sea surface (the boil
775 in 2000 was driven by a $1\text{-}2 \text{ m s}^{-1}$ upwelling - Leifer, Clark, and Chen (2000) - indicates that most emissions are from
776 evasion. A buoyancy plume associated with the rising oil (thick oil slicks surface above the Seep Tents) as well as
777 CH_4 dissolved in the oil likely are transporting the observed, focused CH_4 emissions.

778
779 This is remarkable given that the seep field's geofluid migration "center" in recent decades has been the Seep Tent
780 Seep (Bradley et al., 2010), which was the largest seep in the field in 2010 (Clark et al., 2010). The Seep Tent Seep
781 consists of emissions not captured by the Seep Tents – two large (33-m square) steel capture tents on the seafloor. For
782 reference, the Seep Tents captured $\sim 16,800 \text{ m}^3 \text{ gas dy}^{-1}$ in the early 2000s (Boles et al., 2001). Bradley et al. (2010)
783 found in WCS data that when overall seep field emissions decreased to a minimum in 1995, they were focused on the
784 Seep Tent Seep direction. Note, the Seep Tent Seep was observed first in 1970 as a boil visible from 1.6-km distant.
785 The Seep Tent seep was tented in Sept. 1982 (Boles et al., 2001).

786
787 Underlying these observations are several factors. First, the Seep Tent Seep is modern – since 1978 – as it was not
788 mapped in a 1953 seep survey (Leifer, 2019). At the time it was first reported as a sea boil visible over a kilometer
789 distant (Boles et al., 2001). Since installation, overall Seep Tent production has diminished (Boles et al., 2001) by a
790 factor of 3 from 1984 to 1995. Some fraction of this trend could have resulted from the expansion of active seepage
791 beyond the seep tents. Perhaps more significantly, the Seep Tent Seep lies over one of the Platform Holly wells (Leifer
792 et al., 2010; Fig. 3C), creating the potential of linkage between well production (including stimulation) and Seep Tent
793 production and thus Seep Tent seepage (the uncaptured portion).

794

795 **4.6 Diurnal trend and bias**

796 The diurnal wind patterns typical of the coastal Pacific marine environment are weak offshore (northerly) night winds
797 that shift to from the east in the morning and then swing to from the south. In afternoon they strengthen and shift to
798 prevailing westerlies, continuing to late in the evening (Bradley et al., 2010). Note, WCS seep emissions require winds
799 to "probe or scan" across the seep field, and thus miss the strong afternoon prevailing winds when emissions are
800 expected to be higher. This is because higher wind speeds increase sea-air gas emissions of dissolved near-surface
801 gases (Nightingale et al., 2000) and increase emissions from higher hydrostatic pressure fluctuation driven by wave
802 height (Leifer & Boles, 2005). Given that prevailing winds are westerlies, higher afternoon emissions will generally
803 (but not always) drift eastwards, missing WCS.

804
805 The diurnal wind pattern from the seep field direction is different from the overall (direction-independent) diurnal
806 pattern. Typical nocturnal winds are quite weak, 1.5–1.7 m s⁻¹ (**Fig. 6**). The strongest diurnal wind change was from
807 late night to morning, a 20% decrease. Onshore winds (seep direction) in the middle of the night are from synoptic
808 systems and were associated with the highest C' . Winds increase by a few percent to an early afternoon peak,
809 decreasing through early evening before increasing again later in the night.

810
811 The diurnal trend for C from the seep direction followed the diurnal wind cycle, increasing by ~20 ppb and peaking
812 ~2 hours later in the day than winds (15:00 versus 13:00 for C compared to u , respectively). This may reflect the lag
813 in wave development with respect to wind strengthening and transport time. Based on sensitivity studies, the diurnal
814 cycles in u and C correspond to variations of ~7% and ~9% in E_A .

815
816 Although efforts were made to characterize the diurnal cycle from WCS data, WCS data poorly sample the seep field
817 for the higher wind speeds that occur in the afternoon which primarily are westerlies. Note, non-linearity in sea-air
818 evasion with u means the model use of average u underestimates E_A . Thus, the contribution of the prevailing afternoon
819 winds to diurnal emissions is significantly underestimated from WCS data. It is worth noting, though, that this factor
820 only affects 25-33% of diurnal emissions. As the true diurnal cycle cannot be derived from WCS data, field data of
821 repeat transects spanning the different phases of a diurnal cycle are needed.

822

823 **4.7 Future needs and improvements**

824 The sensitivity studies identified areas for improvement and data gaps. These are described in brief below and in more
825 detail in **Supp. Sec. S8**. The largest uncertainty was with regards to partitioning between the inshore and offshore seep
826 trends, which could be determined by a second air quality station, preferably including speciation such as by CEAS
827 analyzers of CH₄, C₂H₆, and C₃H₈. Further simulations could add grid cells for evasion corresponding to the
828 downcurrent plumes to assess their contribution. The model was limited by available workstation power; however,
829 additional computation power could open improvements such as simulating a range of wind speeds based on the wind
830 speed probability distribution with respect to wind direction, $\phi(u, \theta)$, e.g., Fig. 5.

831
832 Additional field work and data also are needed. Another important sensitivity was to boundary layer height, BL , which
833 varies diurnally and seasonally (Dorman & Winant, 2000) and could be derived from ceilometer data (Münkel, 2007).
834 Another significant concern is afternoon seep field emissions that bypass WCS, which could be addressed by field
835 work and a second air quality station at a different downwind direction from the seep field. Mapping offshore wind
836 fields to characterize wind veering across the seep field is needed to allow simulations to provide insights at the seep
837 area size-scale.

838

839 **5 Conclusions**

840 In this study, data from an onshore air quality station located downwind of a large marine seep field was analysed to
841 derive the three-decade-averaged seep field emissions using an inversion model. The modeled emissions were similar
842 to reported emissions; however, this was coincidental given that prior reported emissions were during a period of field
843 quiescence. Highlighting the significance of the COP seep field, ethane and propane emissions suggest the COP seep
844 field contributes 0.04% and 0.12% of the global seep budget, respectively. As a result, COP seep field emissions of
845 19 Gg CH₄ yr⁻¹ are consistent with global geo-gas budgets of 45 Tg yr⁻¹, but inconsistent with significantly lower
846 emissions estimated from ice core isotopic data. Additionally, the approach could be adapted to air quality station data
847 for other sources including terrestrial seeps, production fields, etc., if the sources are spatially constrained and isolated
848 from confounding sources.

849
850 **Data availability.** All data needed to evaluate the conclusions in the paper are present in the paper and/or the
851 Supplementary Materials and/or were submitted to the Mendeley Data Repository, see Leifer, Ira (2020),
852 “Seep_Air_Data”, Mendeley Data, V1, <http://dx.doi.org/10.17632/znzhxkftm8.1>
853

854 **Supplement.** The supplement contains additional supporting figures and details to complement the manuscript and
855 an interactive map file as a Google Earth archive of the offshore survey data that are presented in **Fig. 2**.

856
857 **Author Contributions.** IL Developed and conducted the study, analysed data, and wrote the manuscript. CM analysed
858 data and edited the manuscript. DB analysed air sample data and edited the manuscript.

859
860 **Competing interests.** The authors declare that they have no conflict of interest.

861
862 **Acknowledgements.** We would like to gratefully acknowledge the SBCAPCD for providing data from their ongoing
863 monitoring program and the contribution of Marc Moritsch and Joel S. Cordes in particular for help with these data,
864 and Doug Wilson for the processed sonar data. We recognize the skill and participation of vessel captains Jeff Wright
865 and Tony Vultaggio and editorial review by Charlotte Marston, Bubbleology Research International.

866
867 **Financial Support.** This work was supported by Plains All American Pipeline and the Bubbleology Research
868 International, Internal Research and Development (IRAD) fund.

869

870 **References**

- 871 Abrams, M. A. (2005). Significance of hydrocarbon seepage relative to petroleum generation and
 872 entrapment. *Marine and Petroleum Geology*, 22(4), 457-477.
 873 doi:10.1016/j.marpetgeo.2004.08.003
- 874 Abrams, M. A. (2017). Evaluation of near-surface gases in marine sediments to assess
 875 subsurface petroleum gas generation and entrapment. *Geosciences*, 7(2), 35.
 876 doi:10.3390/geosciences7020035
- 877 Bernard, B. B., Brooks, J. M., & Zumberge, J. (2001, 16-19 September 2001). *Determining the*
 878 *origin of gases in near-surface sediments*. Paper presented at the AAPG Hedberg
 879 Conference, Vancouver BC, Canada.
- 880 Boles, J. R., Clark, J. F., Leifer, I., & Washburn, L. (2001). Temporal variation in natural
 881 methane seep rate due to tides, Coal Oil Point area, California. *Journal Geophysical*
 882 *Research - Oceans*, 106(C11), 27,077-027,086. doi:10.1029/2000JC000774
- 883 Borges, A. V., Champenois, W., Gypens, N., Delille, B., & Harlay, J. (2016). Massive marine
 884 methane emissions from near-shore shallow coastal areas. *Scientific Reports*, 6, 27908.
 885 doi:10.1038/srep27908
- 886 Bradley, E. S., Leifer, I., & Roberts, D. A. (2010). Long-term monitoring of a marine geologic
 887 hydrocarbon source by a coastal air pollution station in Southern California. *Atmospheric*
 888 *Environment*, 44(38), 4973-4981. doi:10.1016/j.atmosenv.2010.08.010
- 889 CDOGGR. (2018). Well Finder. Retrieved 6 May 2019, from California Department of
 890 Conservation <https://www.conservation.ca.gov/dog/Pages/Wellfinder.aspx>
- 891 Ciotoli, G., Procesi, M., Etiope, G., Fracassi, U., & Ventura, G. (2020). Influence of tectonics on
 892 global scale distribution of geological methane emissions. *Nature Communications*,
 893 11(1), 2305. doi:10.1038/s41467-020-16229-1
- 894 Clark, J. F., Washburn, L., Hornafius, J. S., & Luyendyk, B. P. (2000). Natural marine
 895 hydrocarbon seep source of dissolved methane to California coastal waters. *Journal*
 896 *Geophysical Research - Oceans*, 105, 11,509-511,522. doi:10.1029/2000JC000259
- 897 Clark, J. F., Washburn, L., & Schwager, K. (2010). Variability of gas composition and flux
 898 intensity in natural marine hydrocarbon seeps. *Geo-Marine Letters*, 30, 379-388.
 899 doi:10.1007/s00367-009-0167-1
- 900 Di, P., Feng, D., & Chen, D. (2019). The distribution of dissolved methane and its air-sea flux in
 901 the plume of a seep field, Lingtou Promontory, South China Sea. *Geofluids*, 2019,
 902 3240697. doi:10.1155/2019/3240697
- 903 Di, P., Feng, D., Tao, J., & Chen, D. (2020). Using time-series videos to quantify methane
 904 bubbles flux from natural cold seeps in the South China Sea. *Minerals*, 10(3), 216.
 905 doi:10.3390/min10030216
- 906 Dorman, C. E., & Winant, C. D. (2000). The structure and variability of the marine atmosphere
 907 around the Santa Barbara Channel. *Monthly Weather Review*, 128(2), 261-282.
 908 doi:10.1175/1520-0493(2000)128<0261
- 909 Edinger, J. G. (1959). Changes in the depth of the marine layer over the Los Angeles Basin.
 910 *Journal of Meteorology*, 16(3), 219-226. doi:10.1175/1520-
 911 0469(1959)016<0219:citdot>2.0.co;2
- 912 Etiope, G., & Ciccio, P. (2009). Earth's degassing: A missing ethane and propane source.
 913 *Science*, 323(5913), 478-478. doi:10.1126/science.1165904

914 Etiope, G., Ciotoli, G., Schwietzke, S., & Schoell, M. (2019). Gridded maps of geological
915 methane emissions and their isotopic signature. *Earth System Science Data*, *11*(1), 1-22.
916 doi:10.5194/essd-11-1-2019

917 Etiope, G., & Schwietzke, S. (2019). Global geological methane emissions: An update of top-
918 down and bottom-up estimates. *Elementa: Science of the Anthropocene*, *7*.
919 doi:10.1525/elementa.383

920 Fischer, P. J. (1978). Oil and Tar Seeps, Santa Barbara Basin, California. In D. J. Everitts, R. G.
921 Paul, C. F. Eaton, & E. E. Welday (Eds.), *California Offshore Gas, Oil and Tar Seeps*
922 (pp. 1-62). Sacramento, California: California State Lands Commission.

923 Freeworldmaps (Cartographer). (2020). Physical Map of California. Retrieved from
924 <https://www.freeworldmaps.net/united-states/california/map.html>

925 Frew, N. M., Bock, E. J., Schimpf, U., Hara, T., Haußecker, H., Edson, J. B., . . . Jähne, B.
926 (2004). Air-sea gas transfer: Its dependence on wind stress, small-scale roughness, and
927 surface films. *Journal of Geophysical Research: Oceans*, *109*(C8), C08S17.
928 doi:10.1029/2003JC002131

929 Greinert, J. (2008). Monitoring temporal variability of bubble release at seeps: The
930 hydroacoustic swath system GasQuant. *Journal of Geophysical Research*, *113*, C07048.
931 doi:10.1029/2007JC004704

932 Greinert, J., McGinnis, D. F., Naudts, L., Linke, P., & De Batist, M. (2010). Atmospheric
933 methane flux from bubbling seeps: Spatially extrapolated quantification from a Black Sea
934 shelf area. *Journal of Geophysical Research*, *115*. doi:10.1029/2009jc005381

935 Hanna, S. R., Briggs, G. A., & Hosker Jr., R. P. (1982). *Handbook on Atmospheric Diffusion* (J.
936 S. Smith Ed.): Technical Information Center, U.S. Department of Energy.

937 Helmig, D., Rossabi, S., Hueber, J., Tans, P., Montzka, S. A., Masarie, K., . . . Pozzer, A. (2016).
938 Reversal of global atmospheric ethane and propane trends largely due to US oil and
939 natural gas production. *Nature Geoscience*, *9*(7), 490-495. doi:10.1038/ngeo2721

940 Heyer, J., & Berger, U. (2000). Methane emission from the coastal area in the Southern Baltic
941 Sea. *Estuarine, Coastal and Shelf Science*, *51*(1), 13-30. doi:10.1006/ecs.2000.0616

942 Higgs, B., Mountjoy, J. J., Crutchley, G. J., Townend, J., Ladroit, Y., Greinert, J., & McGovern,
943 C. (2019). Seep-bubble characteristics and gas flow rates from a shallow-water, high-
944 density seep field on the shelf-to-slope transition of the Hikurangi subduction margin.
945 *Marine Geology*, *417*, 105985. doi:10.1016/j.margeo.2019.105985

946 Hmiel, B., Petrenko, V. V., Dyonisius, M. N., Buizert, C., Smith, A. M., Place, P. F., . . .
947 Dlugokencky, E. (2020). Preindustrial 14CH₄ indicates greater anthropogenic fossil CH₄
948 emissions. *Nature*, *578*(7795), 409-412. doi:10.1038/s41586-020-1991-8

949 Höglund-Isaksson, L. (2017). Bottom-up simulations of methane and ethane emissions from
950 global oil and gas systems 1980 to 2012. *Environmental Research Letters*, *12*(2), 024007.
951 doi:10.1088/1748-9326/aa583e

952 Hornafius, S. J., Quigley, D. C., & Luyendyk, B. P. (1999). The world's most spectacular marine
953 hydrocarbons seeps (Coal Oil Point, Santa Barbara Channel, California): Quantification
954 of emissions. *Journal Geophysical Research - Oceans*, *104*(C9), 20,703-720,711.
955 doi:10.1029/1999JC900148

956 Hughes, M., Hall, A., & Fovell, R. G. (2007). Dynamical controls on the diurnal cycle of
957 temperature in complex topography. *Climate Dynamics*, *29*(2), 277-292.
958 doi:10.1007/s00382-007-0239-8

959 IEA. (2020). *Methane Tracker 2020*. Retrieved from Paris: [https://www.iea.org/reports/methane-](https://www.iea.org/reports/methane-tracker-2020)
960 [tracker-2020](https://www.iea.org/reports/methane-tracker-2020)

961 IPCC. (2013). *Working Group I Contribution to the IPCC Fifth Assessment Report Climate*
962 *Change 2013-The Physical Science Basis*. Retrieved from IPCC Secretariat, Geneva,
963 Switzerland:

964 IPCC. (2014). *Climate Change 2014: Synthesis Report. Contributions of Working Groups I, II*
965 *and III to the Fifth Assessment Report of the Intergovernmental Panel on Climate*
966 *Change*. Retrieved from Geneva, Switzerland: [http://www.ipcc.ch/pdf/assessment-](http://www.ipcc.ch/pdf/assessment-report/ar5/syr/SYR_AR5_FINAL_full_wcover.pdf)
967 [report/ar5/syr/SYR_AR5_FINAL_full_wcover.pdf](http://www.ipcc.ch/pdf/assessment-report/ar5/syr/SYR_AR5_FINAL_full_wcover.pdf)

968 Jackson, R. B., Saunio, M., Bousquet, P., Canadell, J. G., Poulter, B., Stavert, A. R., . . .
969 Tsuruta, A. (2020). Increasing anthropogenic methane emissions arise equally from
970 agricultural and fossil fuel sources. *Environmental Research Letters*, 15(7), 071002.
971 doi:10.1088/1748-9326/ab9ed2

972 Johansen, C., Macelloni, L., Natter, M., Silva, M., Woosley, M., Woolsey, A., . . . MacDonald, I.
973 R. (2020). Hydrocarbon migration pathway and methane budget for a Gulf of Mexico
974 natural seep site: Green Canyon 600. *Earth and Planetary Science Letters*, 545, 116411.
975 doi:10.1016/j.epsl.2020.116411

976 Johansen, C., Todd, A. C., & MacDonald, I. R. (2017). Time series video analysis of bubble
977 release processes at natural hydrocarbon seeps in the Northern Gulf of Mexico. *Marine*
978 *and Petroleum Geology*, 82, 21-34. doi:[10.1016/j.marpetgeo.2017.01.014](https://doi.org/10.1016/j.marpetgeo.2017.01.014)

979 Jordan, S. F. A., Treude, T., Leifer, I., Janßen, R., Werner, J., Schulz-Vogt, H., & Schmale, O.
980 (2020). Bubble-mediated transport of benthic microorganisms into the water column:
981 Identification of methanotrophs and implication of seepage intensity on transport
982 efficiency. *Scientific Reports*, 10(1), 4682. doi:10.1038/s41598-020-61446-9

983 Judd, A., & Hovland, M. (2007). *Seabed fluid flow: The impact on geology, biology and the*
984 *marine environment*. Cambridge, UK: Cambridge University Press.

985 Kasaya, T., Mitsuzawa, K., Goto, T.-n., Iwase, R., Sayanagi, K., Araki, E., . . . Nagao, T. (2009).
986 Trial of multidisciplinary observation at an expandable sub-marine cabled station “Off-
987 Hatsushima Island Observatory” in Sagami Bay, Japan. *Sensors*, 9(11), 9241-9254.
988 doi:10.3390/s91109241

989 Leifer, I. (2010). Characteristics and scaling of bubble plumes from marine hydrocarbon seepage
990 in the Coal Oil Point seep field. *Journal Geophysical Research*, 115(C11), C11014.
991 doi:10.1029/2009JC005844

992 Leifer, I. (2015). Seabed bubble flux estimation by calibrated video survey for a large blowout
993 seep in the North Sea. *Journal of Marine and Petroleum Geology*, 68B, 743-752.
994 doi:10.1016/j.marpetgeo.2015.08.032

995 Leifer, I. (2019). A synthesis review of emissions and fates for the Coal Oil Point marine
996 hydrocarbon seep field and California marine seepage. *Geofluids*, 2019(4724587), 1-48.
997 doi:10.1155/2019/4724587

998 Leifer, I., & Boles, J. (2005). Turbine tent measurements of marine hydrocarbon seeps on
999 subhourly timescales. *Journal of Geophysical Research-Oceans*, 110(C1), C01006.
1000 doi:10.1029/2003jc002207

1001 Leifer, I., Boles, J. R., Luyendyk, B. P., & Clark, J. F. (2004). Transient discharges from marine
1002 hydrocarbon seeps: Spatial and temporal variability. *Environmental Geology*, 46(8),
1003 1038-1052. doi:10.1007/s00254-004-1091-3

- 1004 Leifer, I., Chernykh, D., Shakhova, N., & Semiletov, I. (2017). Sonar gas flux estimation by
1005 bubble insonification: Application to methane bubble flux from seep areas in the outer
1006 Laptev Sea. *The Cryosphere*, 11(3), 1333-1350. doi:10.5194/tc-11-1333-2017
- 1007 Leifer, I., & Clark, J. F. (2002). Modeling trace gases in hydrocarbon seep bubbles: Application
1008 to marine hydrocarbon seeps in the Santa Barbara Channel. *Geologiya I Geofizika*, 47(7),
1009 572-579.
- 1010 Leifer, I., Clark, J. F., & Chen, R. F. (2000). Modifications of the local environment by natural
1011 marine hydrocarbon seeps. *Geophysical Research Letters*, 27(22), 3711-3714.
1012 doi:10.1029/2000GL011619
- 1013 Leifer, I., Jeuthé, H., Gjørund, S. H., & Johansen, V. (2009). Engineered and natural marine
1014 seep, bubble-driven buoyancy flows. *Journal of Physical Oceanography*, 39(12), 3071-
1015 3090. doi:10.1175/2009JPO4135.1
- 1016 Leifer, I., Kamerling, M., Luyendyk, B. P., & Wilson, D. (2010). Geologic control of natural
1017 marine hydrocarbon seep emissions, Coal Oil Point seep field, California. *Geo-Marine*
1018 *Letters*, 30(3-4), 331-338. doi:10.1007/s00367-010-0188-9
- 1019 Leifer, I., Luyendyk, B. P., Boles, J., & Clark, J. F. (2006). Natural marine seepage blowout:
1020 Contribution to atmospheric methane. *Global Biogeochemical Cycles*, 20(3), GB3008.
1021 doi:10.1029/2005GB002668
- 1022 Leifer, I., & MacDonald, I. (2003). Dynamics of the gas flux from shallow gas hydrate deposits:
1023 interaction between oily hydrate bubbles and the oceanic environment. *Earth and*
1024 *Planetary Science Letters*, 210(3-4), 411-424. doi:10.1016/S0012-821X(03)00173-0
- 1025 Leifer, I., Melton, C., Fischer, M. L., Fladeland, M., Frash, J., Gore, W., . . . Yates, E. L. (2018).
1026 Atmospheric characterization through fused mobile airborne and surface in situ surveys:
1027 Methane emissions quantification from a producing oil field. *Atmospheric Measurement*
1028 *Techniques*, 11(3), 1689-1705. doi:10.5194/amt-11-1689-2018
- 1029 Leifer, I., Melton, C., Manish, G., & Leen, B. (2014). Mobile monitoring of methane leakage.
1030 *Gases and Instrumentation*, July/August 2014, 20-24.
- 1031 Leifer, I., Melton, C., Tratt, D. M., Buckland, K. N., Chang, C., Frash, J., . . . Yurganov, L.
1032 (2018). Validation of mobile in situ measurements of dairy husbandry emissions by
1033 fusion of airborne/surface remote sensing with seasonal context from the Chino Dairy
1034 Complex. *Environmental Pollution*, 242(Pt B), 2111-2134.
1035 doi:10.1016/j.envpol.2018.03.078
- 1036 Leifer, I., Melton, C., Tratt, D. M., Buckland, K. N., Clarisse, L., Coheur, P., . . . Yurganov, L.
1037 (2016). Remote sensing and in situ measurements of methane and ammonia emissions
1038 from a megacity dairy complex: Chino, CA. *Environmental Pollution*, 221, 37-51.
1039 doi:10.1016/j.envpol.2016.09.083
- 1040 Leifer, I., & Patro, R. (2002). The bubble mechanism for methane transport from the shallow
1041 seabed to the surface: A review and sensitivity study. *Continental Shelf Research*, 22(16),
1042 2409-2428. doi:10.1016/S0278-4343(02)00065-1
- 1043 Leifer, I., Solomon, E., Schneider v. Deimling, J., Coffin, R., Rehder, G., & Linke, P. (2015).
1044 The fate of bubbles in a large, intense bubble plume for stratified and unstratified water:
1045 Numerical simulations of 22/4b expedition field data. *Journal of Marine and Petroleum*
1046 *Geology*, 68B, 806-823. doi:10.1016/j.marpetgeo.2015.07.025
- 1047 Liss, P. S., & Duce, R. A. (2005). *The sea surface and global change*: Cambridge University
1048 Press.

- 1049 Liss, P. S., & Merlivat, L. (1986). Air-sea gas exchange rates: Introduction and synthesis. In P.
1050 Buat-Ménard (Ed.), *The Role of Air-Sea Exchange in Geochemical Cycling* (Vol. 185).
1051 Dordrecht: Springer.
- 1052 Lu, R., Turco, R. P., & Jacobson, M. Z. (1997). An integrated air pollution modeling system for
1053 urban and regional scales: 1. Structure and performance. *Journal of Geophysical*
1054 *Research: Atmospheres*, 102(D5), 6063-6079. doi:10.1029/96jd03501
- 1055 Marinaro, G., Etiope, G., Bue, N. L., Favali, P., Papatheodorou, G., Christodoulou, D., . . . Rolin,
1056 J.-F. (2006). Monitoring of a methane-seeping pockmark by cabled benthic observatory
1057 (Patras Gulf, Greece). *Geo-Marine Letters*, 26(5), 297-302. doi:10.1007/s00367-006-
1058 0040-4
- 1059 Mazzini, A., Sciarra, A., Etiope, G., Sadavarte, P., Houweling, S., Pandey, S., & Husein, A.
1060 (2021). Relevant methane emission to the atmosphere from a geological gas
1061 manifestation. *Scientific Reports*, 11(1), 4138. doi:10.1038/s41598-021-83369-9
- 1062 Minor, S. A., Kellogg, K. S., Stanley, R. G., Gurrola, L. D., Keller, E. A., & Brandt, T. R.
1063 (Cartographer). (2009). Geologic Map of the Santa Barbara Coastal Plain Area, Santa
1064 Barbara County, California. Retrieved from <https://pubs.usgs.gov/sim/3001/>
- 1065 Munkel, C. (2007). Mixing height determination with lidar ceilometers - Results from Helsinki
1066 Testbed. *Meteorologische Zeitschrift*, 16, 451-459. doi:10.1127/0941-2948/2007/0221
- 1067 Muyakshin, S. I., & Sauter, E. (2010). The hydroacoustic method for the quantification of the gas
1068 flux from a submersed bubble plume. *Oceanology*, 50(6), 995-1001.
1069 doi:10.1134/S0001437010060202
- 1070 Nicewonger, M. R., Verhulst, K. R., Aydin, M., & Saltzman, E. S. (2016). Preindustrial
1071 atmospheric ethane levels inferred from polar ice cores: A constraint on the geologic
1072 sources of atmospheric ethane and methane. *Geophysical Research Letters*, 43(1), 214-
1073 221. doi:<https://doi.org/10.1002/2015GL066854>
- 1074 Nightingale, P. D., Malin, G., Law, C. S., Watson, A. J., Liss, P. S., Liddicoat, M. I., . . . Upstill-
1075 Goddard, R. C. (2000). In situ evaluation of air-sea gas exchange parameterizations using
1076 novel conservative and volatile tracers. *Global Biogeochemical Cycles*, 14(1), 373-387.
1077 doi:10.1029/1999GB900091
- 1078 Nisbet, E. G., Manning, M. R., Dlugokencky, E. J., Fisher, R. E., Lowry, D., Michel, S. E., . . .
1079 White, J. W. C. (2019). Very strong atmospheric methane growth in the 4 years 2014–
1080 2017: Implications for the Paris Agreement. *Global Biogeochemical Cycles*, 33(3), 318-
1081 342. doi:10.1029/2018GB006009
- 1082 Olson, D. J. (1983). *Surface and subsurface geology of the Santa Barbara Goleta Metropolitan*
1083 *area, Santa Barbara County, California*. (MS). Oregon State University, Retrieved from
1084 [https://ir.library.oregonstate.edu/concern/graduate_thesis_or_dissertations/v692tb957?loc](https://ir.library.oregonstate.edu/concern/graduate_thesis_or_dissertations/v692tb957?locale=it)
1085 [ale=it](https://ir.library.oregonstate.edu/concern/graduate_thesis_or_dissertations/v692tb957?locale=it)
- 1086 Padilla, A. M., Loranger, S., Kinnaman, F. S., Valentine, D. L., & Weber, T. C. (2019). Modern
1087 assessment of natural hydrocarbon gas flux at the Coal Oil Point seep field, Santa
1088 Barbara, California. *Journal of Geophysical Research: Oceans*, 124(4), 2472-2484.
1089 doi:10.1029/2018jc014573
- 1090 Peischl, J., Ryerson, T. B., Brioude, J., Aikin, K. C., Andrews, A. E., Atlas, E., . . . Parrish, D. D.
1091 (2013). Quantifying sources of methane using light alkanes in the Los Angeles basin,
1092 California. *Journal of Geophysical Research: Atmospheres*, 118(10), 4974-4990.
1093 doi:10.1002/jgrd.50413

1094 Pozzer, A., Pollmann, J., Taraborrelli, D., Jöckel, P., Helmig, D., Tans, P., . . . Lelieveld, J.
1095 (2010). Observed and simulated global distribution and budget of atmospheric C₂-C₅
1096 alkanes. *Atmospheric Chemistry and Physics*, 10(9), 4403-4422. doi:10.5194/acp-10-
1097 4403-2010

1098 Rahn, D. A., Parish, T. R., & Leon, D. (2017). Synthesis of observations from the Precision
1099 Atmospheric Marine Boundary Layer Experiment (PreAMBLE). *Monthly Weather*
1100 *Review*, 145(6), 2325-2342. doi:10.1175/mwr-d-16-0373.1

1101 Reeburgh, W. S. (2007). Oceanic methane biogeochemistry. *Chemical Reviews*, 107(2), 486-513.
1102 doi:10.1021/cr050362v

1103 Reeburgh, W. S., Ward, B. B., Whalen, S. C., Sandbeck, K. A., Kilpatrick, K. A., & Kerkhof, L.
1104 J. (1991). Black Sea methane geochemistry. *Deep Sea Research Part A. Oceanographic*
1105 *Research Papers*, 38, S1189-S1210. doi:[10.1016/S0198-0149\(10\)80030-5](https://doi.org/10.1016/S0198-0149(10)80030-5)

1106 Rehder, G., Keir, R. S., Suess, E., & Rhein, M. (1999). Methane in the Northern Atlantic
1107 controlled by microbial oxidation and atmospheric history. *Geophysical Research*
1108 *Letters*, 26(5), 587-590. doi:10.1029/1999GL900049

1109 Riedel, M., Scherwath, M., Römer, M., Veloso, M., Heesemann, M., & Spence, G. D. (2018).
1110 Distributed natural gas venting offshore along the Cascadia margin. *Nature*
1111 *Communications*, 9(1), 3264. doi:10.1038/s41467-018-05736-x

1112 Römer, M., Hsu, C.-W., Loher, M., MacDonald, I. R., dos Santos Ferreira, C., Pape, T., . . .
1113 Sahling, H. (2019). Amount and fate of gas and oil discharged at 3400 m water depth
1114 from a natural seep site in the Southern Gulf of Mexico. *Frontiers in Marine Science*,
1115 6(700). doi:10.3389/fmars.2019.00700

1116 Römer, M., Riedel, M., Scherwath, M., Heesemann, M., & Spence, G. D. (2016). Tidally
1117 controlled gas bubble emissions: A comprehensive study using long-term monitoring data
1118 from the NEPTUNE cabled observatory offshore Vancouver Island. *Geochemistry*,
1119 *Geophysics, Geosystems*, 17(9), 3797-3814. doi:10.1002/2016GC006528

1120 Römer, M., Sahling, H., Pape, T., Bohrmann, G., & Spieß, V. (2012). Quantification of gas
1121 bubble emissions from submarine hydrocarbon seeps at the Makran continental margin
1122 (offshore Pakistan). *Journal of Geophysical Research: Oceans*, 117(C10), C10015.
1123 doi:10.1029/2011jc007424

1124 Römer, M., Wenau, S., Mau, S., Veloso, M., Greinert, J., Schlüter, M., & Bohrmann, G. (2017).
1125 Assessing marine gas emission activity and contribution to the atmospheric methane
1126 inventory: A multidisciplinary approach from the Dutch Dogger Bank seep area (North
1127 Sea). *Geochemistry, Geophysics, Geosystems*, 18(7), 2617-2633.
1128 doi:10.1002/2017gc006995

1129 Saunio, M., Stavert, A. R., Poulter, B., Bousquet, P., Canadell, J. G., Jackson, R. B., . . .
1130 Zhuang, Q. (2020). The global methane budget 2000-2017. *Earth System Science Data*,
1131 12(3), 1561-1623. doi:10.5194/essd-2019-128

1132 Sauter, E. J., Muyakshin, S. I., Charlou, J.-L., Schlüter, M., Boetius, A., Jerosch, K., . . . Klages,
1133 M. (2006). Methane discharge from a deep-sea submarine mud volcano into the upper
1134 water column by gas hydrate-coated methane bubbles. *Earth and Planetary Science*
1135 *Letters*, 243(3-4), 354-365. doi:10.1016/j.epsl.2006.01.041

1136 Scherwath, M., Thomsen, L., Riedel, M., Römer, M., Chatzievangelou, D., Schwendner, J., . . .
1137 Heesemann, M. (2019). Ocean observatories as a tool to advance gas hydrate research.
1138 *Earth and Space Science*, 6(12), 2644-2652. doi:10.1029/2019ea000762

- 1139 Schmale, O., Beaubien, S. E., Rehder, G., Greinert, J., & Lonmbardi, S. (2010). Gas seepage in
1140 the Dnepr paleo-delta area (NW-Black Sea) and its regional impact on the water column
1141 methane cycle. *Journal of Marine Systems*, 80(1-2), 90-100.
1142 doi:10.1016/j.jmarsys.2009.10.003
- 1143 Schmale, O., Greinert, J., & Rehder, G. (2005). Methane emission from high-intensity marine
1144 gas seeps in the Black Sea into the atmosphere. *Geophysical Research Letters*, 32(7),
1145 L07609. doi:10.1029/2004gl021138
- 1146 Schmale, O., Leifer, I., Stolle, C., Schneider von Deimling, J., Krause, S., Kießlich, K., . . .
1147 Treude, T. (2015). Bubble transport mechanism: Indications for a gas bubble-mediated
1148 inoculation of benthic methanotrophs into the water column. *Continental Shelf*
1149 *Research*, 103, 70-78. doi:10.1016/j.csr.2015.04.022
- 1150 Schneider von Deimling, J., Rehder, G., Greinert, J., McGinnis, D. F., Boetius, A., & Linke, P.
1151 (2011). Quantification of seep-related methane gas emissions at Tommeliten, North Sea.
1152 *Continental Shelf Research*, 31, 867-878. doi:10.1016/j.csr.2011.02.012
- 1153 Schwietzke, S., Sherwood, O. A., Bruhwiler, L. M. P., Miller, J. B., Etiope, G., Dlugokencky, E.
1154 J., . . . Tans, P. P. (2016). Upward revision of global fossil fuel methane emissions based
1155 on isotope database. *Nature*, 538(7623), 88-91. doi:10.1038/nature19797
- 1156 Shakhova, N., Semiletov, I., Leifer, I., Rekant, P., Salyuk, A., & Kosmach, D. (2010).
1157 Geochemical and geophysical evidence of methane release over the East Siberian Arctic
1158 Shelf. *Journal of Geophysical Research*, 115(C8), C08007. doi:10.1029/2009JC005602
- 1159 Shakhova, N., Semiletov, I., Salyuk, A., Iossoupov, V., Kosmach, D., & Gustafsson, O. (2010).
1160 Extensive methane venting to the atmosphere from sediments of the East Siberian Arctic
1161 Shelf. *Science*, 327, 1246-1249. doi:10.1126/science.1182221
- 1162 Shakhova, N., Semiletov Igor P., Leifer, I., Sergienko, V., Salyuk, A., Kosmach, D., . . .
1163 Gustafsson, O. (2013). Ebullition and storm-induced methane release from the East
1164 Siberian Arctic Shelf. *Nature Geoscience*, 7, 64-70. doi:10.1038/ngeo2007
- 1165 Shindell, D. T., Faluvegi, G., Bell, N., & Schmidt, G. A. (2005). An emissions-based view of
1166 climate forcing by methane and tropospheric ozone. *Geophysical Research Letters*, 32,
1167 L04803. doi:10.1029/2004GL021900
- 1168 Simpson, I. J., Sulbaek Andersen, M. P., Meinardi, S., Bruhwiler, L., Blake, N. J., Helmig, D., . . .
1169 . Blake, D. R. (2012). Long-term decline of global atmospheric ethane concentrations and
1170 implications for methane. *Nature*, 488(7412), 490-494. doi:10.1038/nature11342
- 1171 Solomon, E., Kastner, M., MacDonald, I. R., & Leifer, I. (2009). Considerable methane fluxes to
1172 the atmosphere from hydrocarbon seeps in the Gulf of Mexico. *Nature Geoscience*, 2,
1173 561-565. doi:10.1038/NCEO574
- 1174 Thompson, D., Leifer, I., Bovensman, H., Eastwood, M., Fladeland, M., Frankenberg, C., . . .
1175 Thorpe, A. K. (2015). Real-time remote detection and measurement for airborne imaging
1176 spectroscopy: A case study with methane. *Atmospheric Measurement Techniques*, 8, 1-
1177 46. doi:10.5194/amtd-8-1-2015
- 1178 Thornton, B. F., Prytherch, J., Andersson, K., Brooks, I. M., Salisbury, D., Tjernström, M., &
1179 Crill, P. M. (2020). Shipborne eddy covariance observations of methane fluxes constrain
1180 Arctic sea emissions. *Science Advances*, 6(5), eaay7934. doi:10.1126/sciadv.aay7934
- 1181 Veloso-Alarcón, M. E., Jansson, P., De Batist, M., Minshull, T. A., Westbrook, G. K., Pälke, H.,
1182 . . . Greinert, J. (2019). Variability of acoustically evidenced methane bubble emissions
1183 offshore Western Svalbard. *Geophysical Research Letters*, 46(15), 9072-9081.
1184 doi:10.1029/2019gl082750

1185 Wanninkhof, R., Asher, W. E., Ho, D. T., Sweeney, C., & McGillis, W. R. (2009). Advances in
1186 quantifying air-sea gas exchange and environmental forcing. *Annual Review of Marine*
1187 *Science*, 1(1), 213-244. doi:10.1146/annurev.marine.010908.163742

1188 Washburn, L., Johnson, C., Gotschalk, C. G., & Eglund, E. T. (2001). A gas capture buoy for
1189 measuring bubbling gas flux in oceans and lakes. *Journal of Atmospheric and Oceanic*
1190 *Technology*, 18, 1411-1420. doi:10.1175/1520-0426

1191 Weber, D., Marquez, B. A., Taylor, C., Raya, P., Contreras, P., Howard, D., . . . Doezema, L. A.
1192 (2017). Macroseepage of methane and light alkanes at the La Brea tar pits in Los
1193 Angeles. *Journal of Atmospheric Chemistry*, 74(3), 339-356. doi:10.1007/s10874-016-
1194 9346-4

1195 Weber, T. C., Mayer, L., Jerram, K., Beaudoin, J., Rzhanov, Y., & Lovalvo, D. (2014). Acoustic
1196 estimates of methane gas flux from the seabed in a 6000 km² region in the Northern Gulf
1197 of Mexico. *Geochemistry, Geophysics, Geosystems*, 15(5), 1911-1925.
1198 doi:10.1002/2014gc005271

1199 Wiggins, S. M., Leifer, I., Linke, P., & Hildebrand, J. A. (2015). Long-term acoustic monitoring
1200 at North Sea well site 22/4b. *Journal of Marine and Petroleum Geology*, 68, 776-788.
1201 doi:10.1016/j.marpetgeo.2015.02.011

1202 Wilson, D., Leifer, I., & Maillard, E. (2015). Megaplume bubble process visualization by 3D
1203 multibeam sonar mapping. *Journal of Marine and Petroleum Geology*, 68B, 753-765.
1204 doi:10.1016/j.marpetgeo.2015.07.007

1205 Zhao, D., Toba, Y., Suzuki, Y., & Komori, S. (2003). Effect of wind waves on air-sea gas
1206 exchange: Proposal of an overall CO₂ transfer velocity formula as a function of breaking-
1207 wave parameter. *Tellus B: Chemical and Physical Meteorology*, 55(2), 478-487.
1208 doi:10.3402/tellusb.v55i2.16747

1209 Zhao, Y., Saunio, M., Bousquet, P., Lin, X., Berchet, A., Hegglin, M. I., . . . Zheng, B. (2020).
1210 Influences of hydroxyl radicals (OH) on top-down estimates of the global and regional
1211 methane budgets. *Atmospheric Chemistry Physics*, 20(15), 9525-9546. doi:10.5194/acp-
1212 20-9525-2020

1213

1214 **Table of Nomenclature**

1215	NMHC	Non Methane Hydro Carbons
1216	O&G	Oil and Gas
1217	TC	Total Carbon
1218	THC	Total HydroCarbon
1219	WCS	West Campus Station
1220	$C_{ave}(\theta)$	Wind direction-resolved average concentration
1221	C_{CH_4}	Methane concentration
1222	$C_{max}(\theta)$	Wind direction-resolved maximum concentration
1223	$C_{med}(\theta)$	Wind direction-resolved median concentration
1224	C'_{Obs}	WCS observed concentration
1225	C_{seep}	Concentration in seep directions
1226	C'_{Sim}	WCS simulated concentration
1227	$u_{ave}(\theta)$	Wind direction-resolved average u
1228	$u_{max}(\theta)$	Wind direction-resolved maximum u
1229	$u_{med}(\theta)$	Wind direction-resolved median u
1230	u_{seep}	Wind speed in seep directions
1231	BL	Boundary layer height
1232	C	Concentration
1233	$C(t, \theta)$	Wind direction and time-resolved average concentration
1234	C'	Plume (anomaly) concentration
1235	C_1-C_6	Methane to hexane concentrations
1236	E_A	Atmospheric emissions
1237	E_B	Seabed (bottom) emissions
1238	$E_{i,j}$	Grid cell i, j atmospheric emissions
1239	E_W	Emissions to the water column in the near field
1240	i	Grid cell easting index
1241	j	Grid cell northing index
1242	$K(r, \theta)$	Wind direction and distance-resolved correction function to emissions
1243	$K(\theta)$	Wind direction varying, distance correction function to emissions
1244	r	Distance from WCS to cell i, j
1245	R	Residual in C' after Gaussian functional fit
1246	R^2	Correlation coefficient
1247	t	Time
1248	u	Wind speed
1249	$u(\theta)$	Wind direction-resolved wind speed
1250	x, y	Cartesian coordinate system in wind reference frame
1251	Y	Northing offset of WCS
1252	$\delta\theta$	Model wind direction angular resolution
1253	$\phi(u)$	Wind probability distribution
1254	$\phi(\theta, C)$	Wind direction and concentration-resolved probability distribution
1255	$\phi(\theta, u)$	Wind direction and wind speed-resolved probability distribution
1256	$\phi(\omega)$	Sonar return probability distribution
1257	$\phi_i(E_A)$	Normalized atmospheric emissions probability
1258	$\phi_i(\omega)$	Normalized sonar return probability distribution
1259	θ	Wind direction
1260	ω	Sonar return
1261	ψ	Wind veering
1262	ζ	Relative inshore and offshore emissions
1263		

1264 **Table 1. Atmospheric plume composition and model atmospheric emissions.**

1265

1266	Gas	<i>THC</i> Fraction	<i>TC</i> * Fraction	Emissions	Emissions
1267		(%)	(%)	(m ³ dy ⁻¹)	(Mg yr ⁻¹)
1267	CH ₄	88.5	72.8	73,900	19,300
1268	C ₂ H ₆	3.10	2.55	2,590	1270
1269	C ₃ H ₈	4.18	3.44	3,510	2520
1270	C ₄ H ₁₀	2.76	2.27	2,300	2180
1271	C ₅ H ₁₂	1.11	0.92	930	1090
1272	C ₆ H ₁₄	0.133	0.11	110	150
1273	C ₆ H ₆	7.8x10 ⁻⁵	6.4x10 ⁻⁵	7.1	8.3
1274	C ₇ H ₁₆	0.036	0.030	29.7	45.8
1275	C ₇ H ₈	1.8x10 ⁻⁵	1.5x10 ⁻⁵	1.8	2.3
1276	NMHC**	11.5	9.48	9,640	7410
1277	<i>THC</i> ***	85	82.3	83,400	26,600
1278	CO ₂		17.7	21,600	15200
1279	CO		0.003	3780	2660

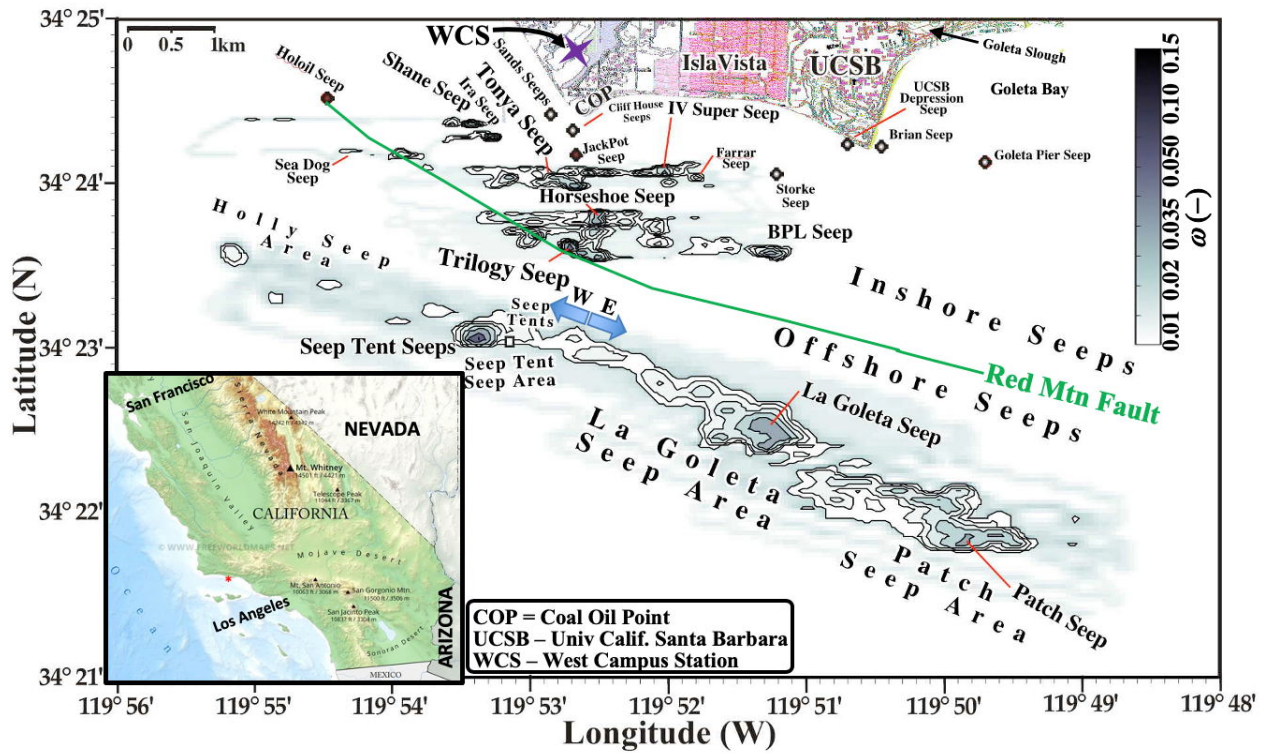
1280

1281 **TC* is total carbon and is *THC*+CO+CO₂

1282 ***NMHC* is non methane hydrocarbons and is C₂-C₇

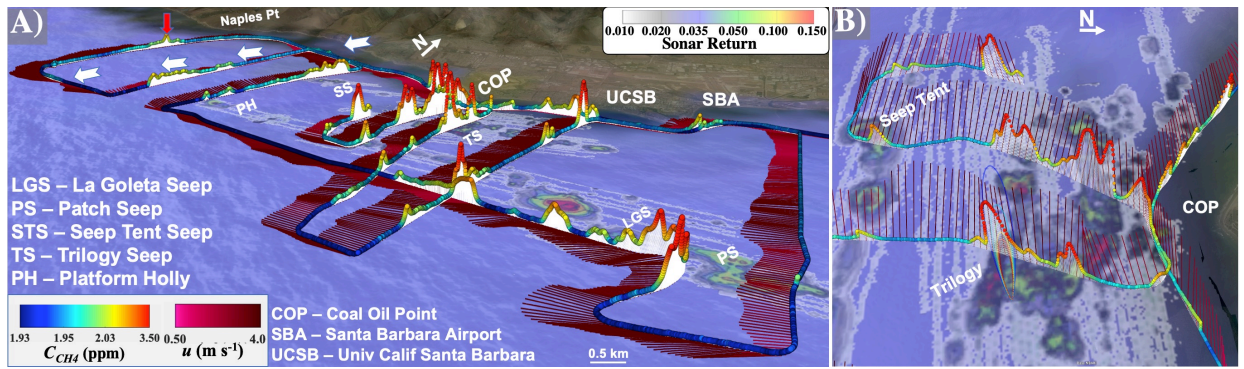
1283 ****THC* is total hydrocarbon and is C₁-C₇

1284



1285
 1286 Figure 1: Sonar return, ω , map after Leifer et al. (2010). Purple star marks West Campus Station (WCS). Seep names are informal
 1287 (Table S3), font size corresponds to strength. E-W arrow segregates east and west offshore seepage. Data keys on panels. Inset
 1288 shows S. California, red dot marks COP seep field. California inset map from Freeworldmaps (2020).

1289



1290

1291

1292

1293

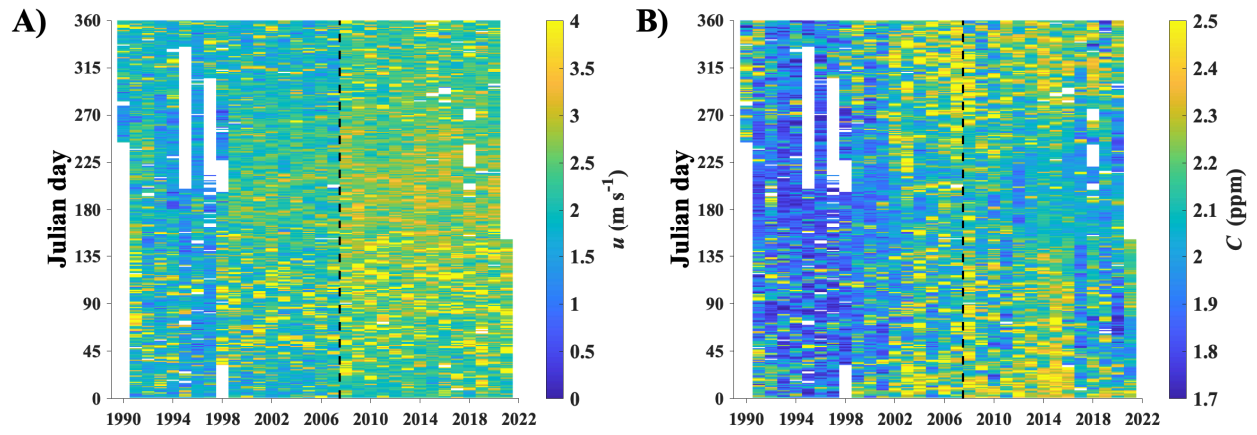
1294

1295

1296

Figure 2: A) Methane, C_{CH_4} , and wind, u , data for 28 May 2016. White arrows show canyon offshore flow. Red arrows show unmapped seepage to the west of the COP seep field. B) C_{CH_4} and u showing Gaussian plume model for Trilogy Seep. Sonar return map shown on sea surface. Data key and seep name key on panel. Displayed in the © GoogleEarth environment. See Supp. Fig. S6 for overhead view.

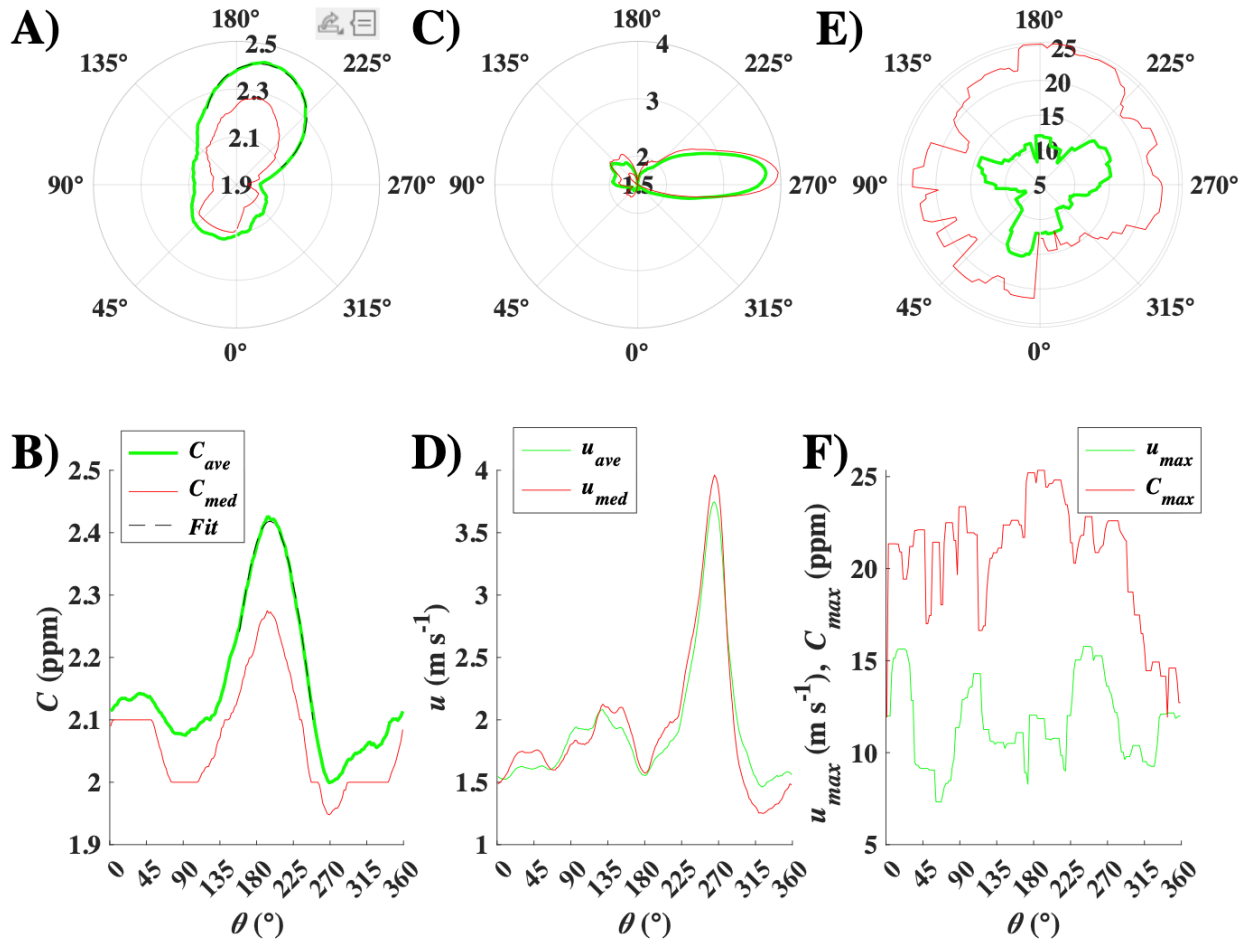
1297



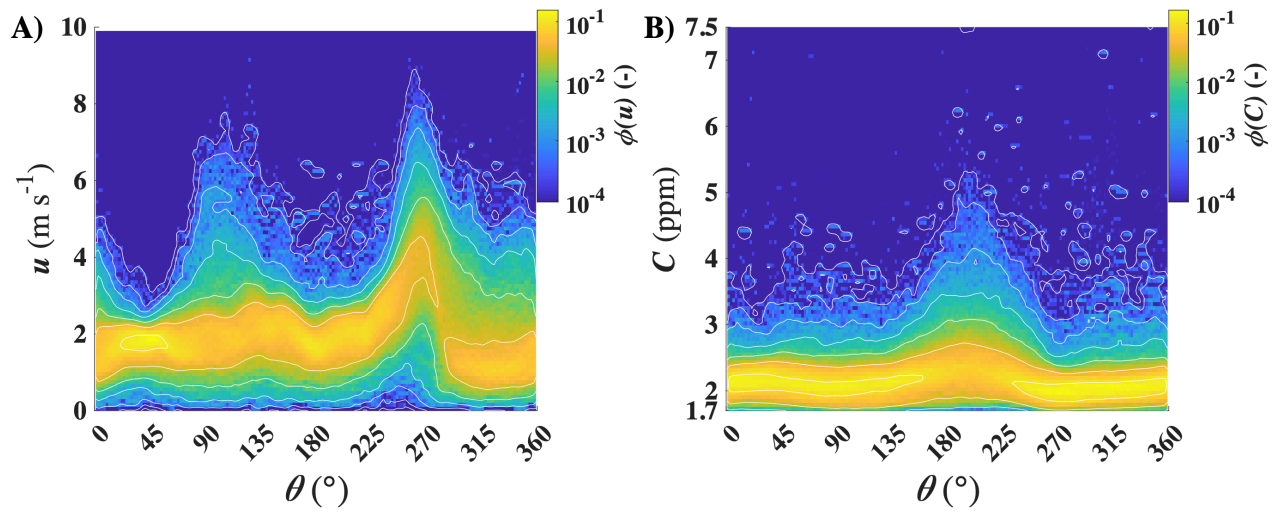
1298
1299
1300

Figure 3: A) Daily mean wind speed, u , and B) concentration, C . Data key on figure. WCS upgrade on Jan 2008 is shown by a dashed black line. Supp. Fig. S7 shows raw dataset.

1301



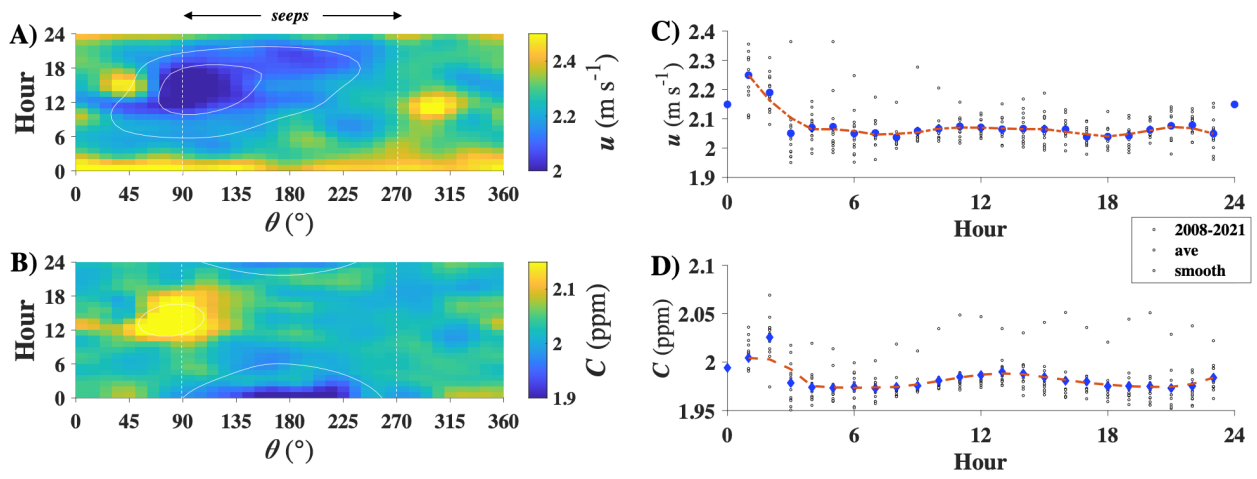
1303
 1304 Figure 4: A, B) Concentration, C , versus wind-direction, θ , 1990-2021 for average, $C_{ave}(\theta)$, and median, $C_{med}(\theta)$, and fit to
 1305 $C_{ave}(\theta)$ for $155 < \theta < 250^\circ$. Data key on panel B. C, D) Wind speed, u , average, $u_{ave}(\theta)$, and median, $u_{med}(\theta)$, Data key on panel
 1306 D. and E, F) Maximum C , $C_{max}(\theta)$, and wind speed, $u_{max}(\theta)$. Data key on panel F. Polar plot oriented as at WCS facing the COP
 1307 seep field.



1309
 1310
 1311
 1312

Figure 5: A) Wind-direction, θ , and wind-speed, u , resolved probability distribution, $\phi(\theta, u)$ and B) Concentration probability distribution, $\phi(\theta, C)$, for 1990-2016. White dashed line shows edges of seep field. Data key on figure.

1313



1314

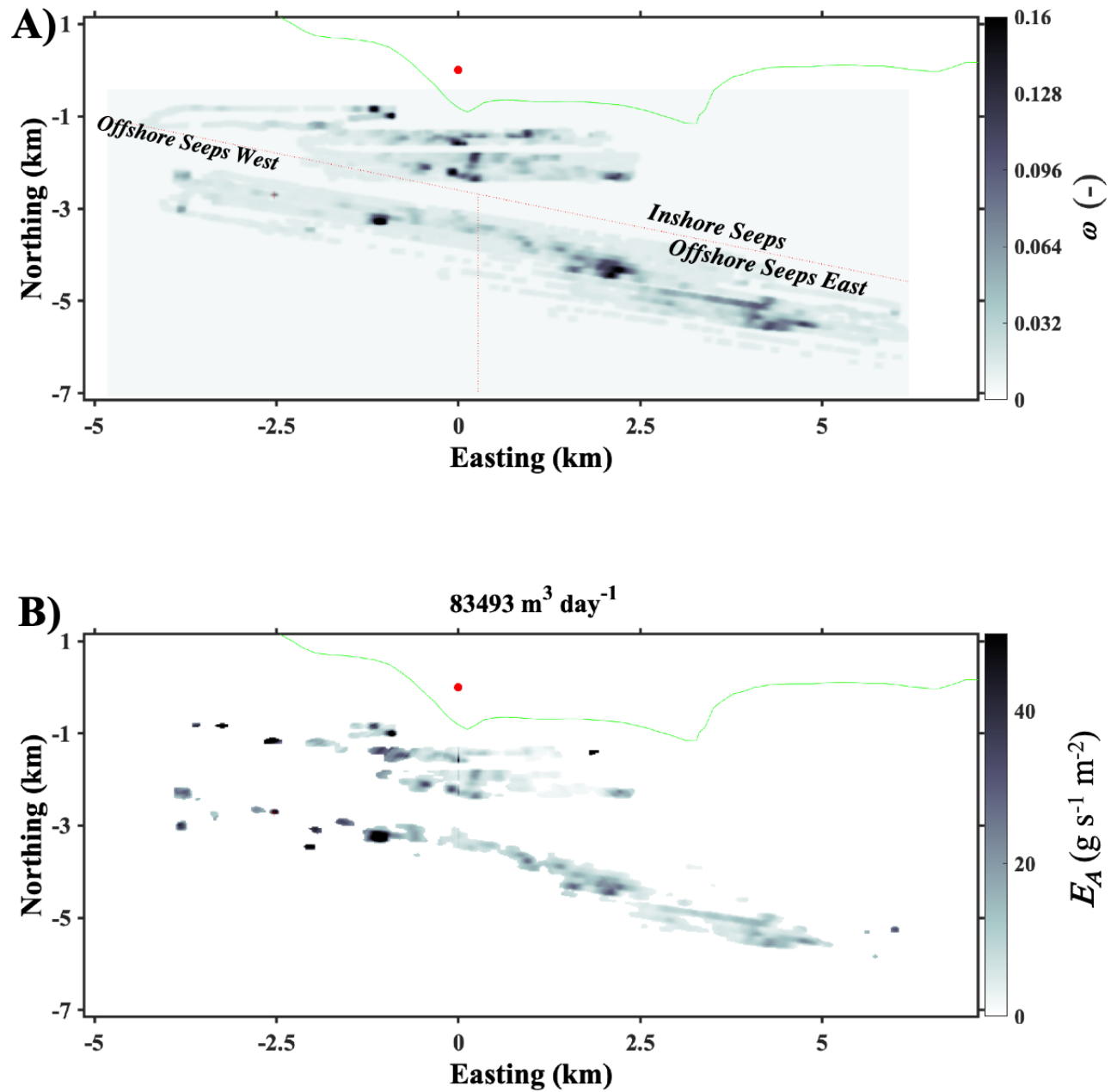
1315

1316

1317

Figure 6: A) 2008–2021 hour- and wind direction-, θ , resolved wind speed, u , and B) concentration, C . C) Hourly-resolved, seep-direction (90–270°), wind speed, u , and D) concentration, C , averaged, individual years, and 3-year smoothed. Data key on figure. Midnight data missing due to daily calibration.

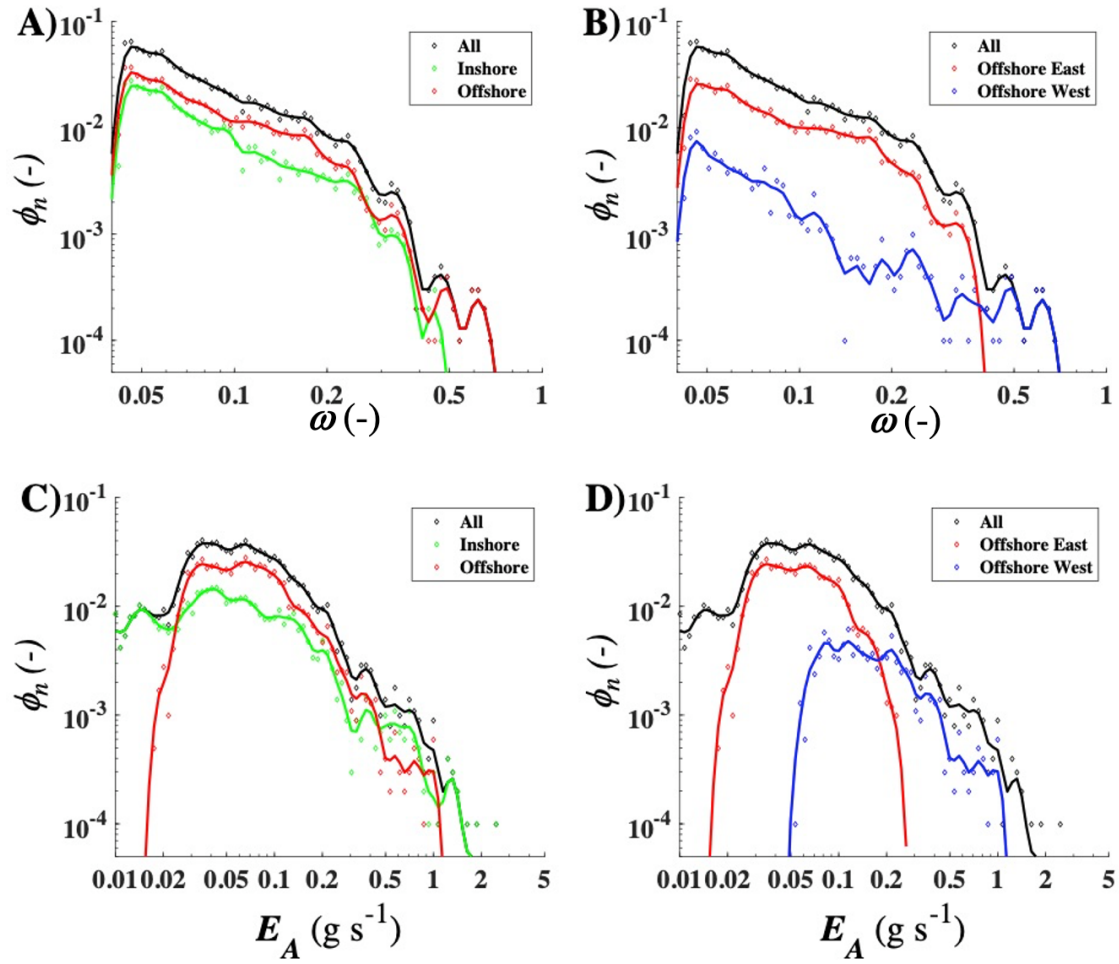
1318



1319
1320
1321

Figure 7: A) Sonar return, ω , gridded at 22-m resolution. B) Atmospheric emissions, E_A . West campus station (red dot) is at coordinate system origin. Green line is coast line.

1322



1323

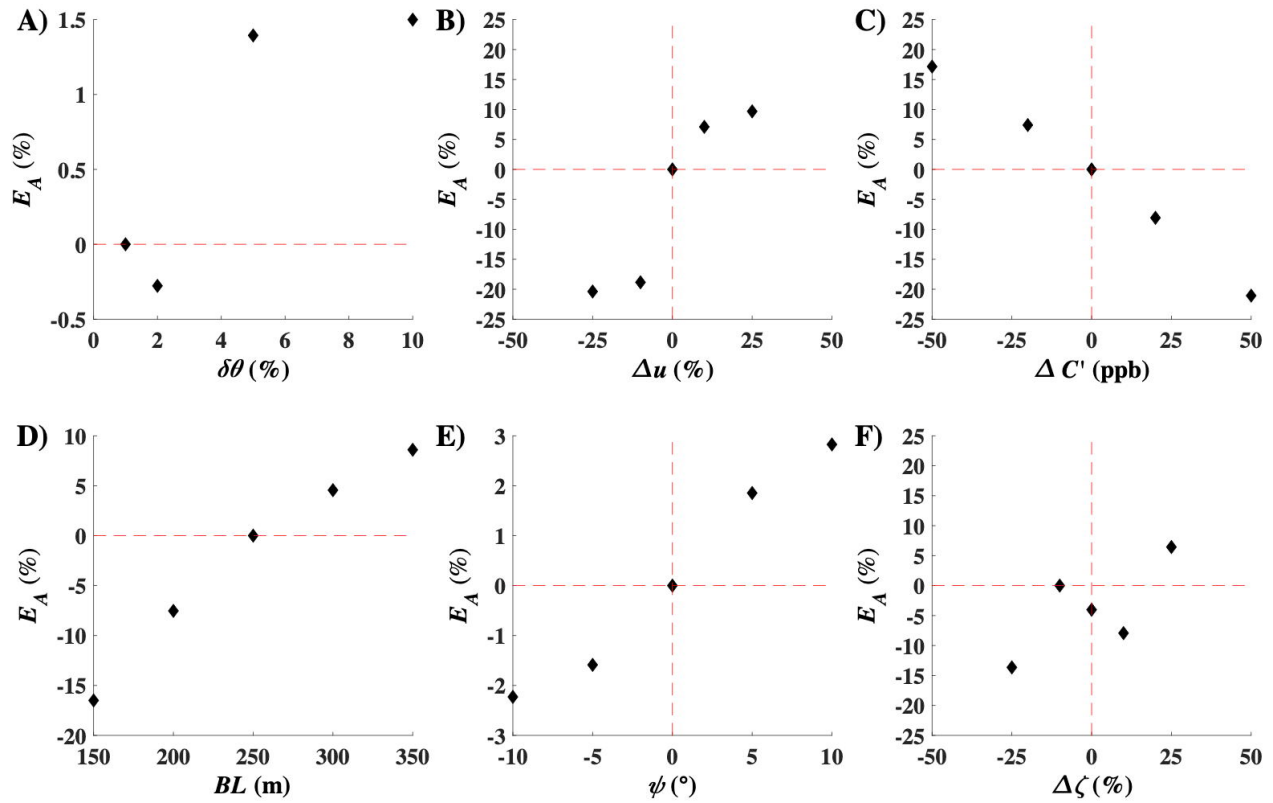
1324

1325

1326

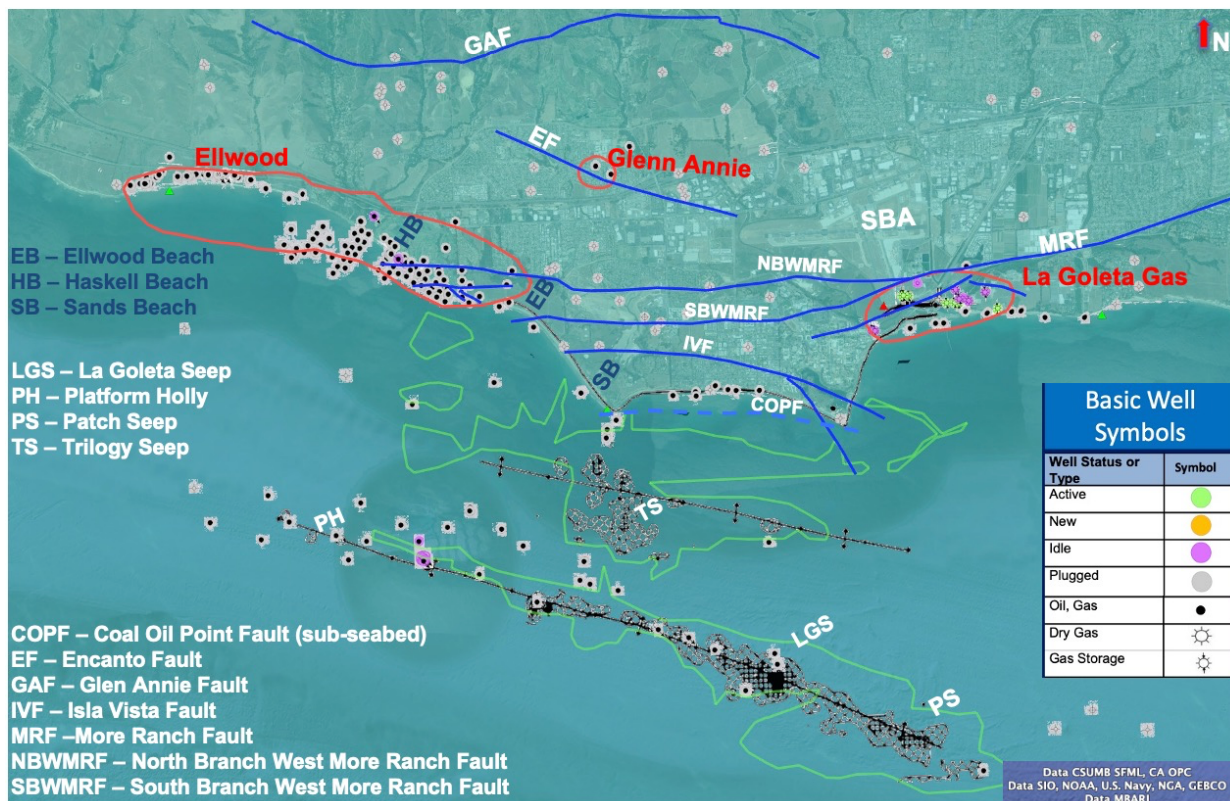
1327

Figure 8: A) Sonar return, ω , occurrence probability, $\phi_n(\omega)$, for all seepage, inshore and offshore seepage and B) all seepage, offshore east seepage, and offshore west seepage. C) Atmospheric emission, E_A , occurrence probability, $\phi_n(E_A)$, for all seepage, inshore and offshore seepage and D) all seepage, offshore east seepage, and offshore west seepage. Data key on panels.



1329
 1330
 1331
 1332

Figure 9: Emissions, E_A , sensitivity to uncertainty in A) model angular resolution, $\delta\theta$, B) wind speed variation, Δu , C) concentration anomaly variation, $\Delta C'$, D) boundary layer thickness, BL , E) wind veering, ψ , and F) inshore/offshore partition variation, $\Delta\zeta$. Note different units on different plots. See text for details.



1333
 1334 Figure 10: Map of the Goleta Plains oil and gas fields, wells, and the Coal Oil Point (COP) seep field. Grey hatch shows 1995 field
 1335 extent, green outlines the 1940 field extent is from Leifer (2019). Field locations from Olson (1983). Well data from CDOGGR
 1336 (2018). Faults from Minor et al. (2009). Seep names are informal. Data keys on panels. Shown in the © Google Earth environment.